Mechanical Systems and Signal Processing 197 (2023) 110362

Contents lists available at ScienceDirect

Mechanical Systems and Signal Processing

journal homepage: www.elsevier.com/locate/ymssp

Exploiting nonlinearity for the design of linear oscillators: Application to an inherently strong nonlinear X-shaped-spring suspension

G. Gatti [a,*], C. Svelto [b]

[a] Dipartimento di Ingegneria Meccanica, Energetica e Gestionale, Università della Calabria, Rende, Italy
[b] Dipartimento di Elettronica, Informazione e Bioingegneria, Politecnico di Milano, Milan, Italy

ARTICLE INFO

Communicated by Xingjian Jing

Keywords:
Vibration isolation
Negative stiffness
Nonlinear damping
Nonlinear stiffness
Quasi-zero stiffness

ABSTRACT

This paper proposes a paradigm shift in the perspective of designing nonlinear oscillators, i.e., the exploitation of nonlinearity to achieve a linear behaviour to good engineering purposes. An elastic suspension with four inclined springs is studied, which has an inherently strong geometric nonlinear stiffness characteristic. Such a configuration has attracted remarkable research efforts in last couple of years, because, compared to other classical nonlinear spring configurations, it has more design parameters, which can be wisely selected to attain a tailored force–displacement characteristic. A particular relationship among these parameters is found so that the overall characteristic becomes exactly linear. Compared to the use of classical linear springs mounted along the direction of motion, the proposed configuration with inclined springs has the potential to allow more freedom in the dimensioning of an engineering device. Also, while the equivalent spring obtained is linear, the equivalent damping is not, and this has the potential advantage of practically realising a linear elastic behaviour with the benefit of geometrical nonlinear damping. Experiments are performed for validation on a prototype device, and results confirm the linear behaviour predicted by the theoretical analysis.

1. Introduction

Nonlinear oscillators have been largely investigated in the last decades to improve the performance of dynamical systems, especially in the field of vibration isolation [1], vibration energy harvesting [2], vibration absorption [3], shock isolation [4], and vibration control problems in general [5].

The classical way in which nonlinearity has been introduced, on purpose, into the design of mechanical systems is by tailoring the stiffness of the elastic suspension by means of specific geometric arrangement of springs and mechanisms [6,7].

Many studies have exploited the combinations of linkages reacting on springs to achieve geometrical nonlinear stiffness, and this has been essentially realised by combining elements of positive and negative stiffness in parallel.

The realization of constant-force (i.e., zero-stiffness) mechanisms has been exploited for robotic automation [8] and to develop quasi-zero stiffness vibration isolators [9].

Diamond structures have been proposed for vibration isolation [10-12], vibration absorption [13], and elastic potential energy

* Corresponding author.
E-mail address: gianluca.gatti@unical.it (G. Gatti).

https://doi.org/10.1016/j.ymssp.2023.110362
Received 20 December 2022; Received in revised form 24 February 2023; Accepted 9 April 2023
Available online 27 April 2023

storage and release [14]. Scissor-like or X-shaped-link structures have been proposed for vibration isolation [15-18], vibration absorption [19], and for metamaterials [20]. To enhance vibration isolation performance, linkages and springs have also been combined in several other ways [21], inspired by limbs [22-24], paws [25,26], cockroaches [27], and biological systems in general [28,29]. Similar archetypes have been proposed to realise vibration dampers [30].

Nonlinear force–displacement curves have also been realised by simply connecting linear springs arranged in a geometric configuration. The idea of using one pair of linear springs orthogonal to the direction of motion, which incline as the suspended mass moves [31], was studied and investigated to realise quasi-zero stiffness force–displacement characteristics and implement effective vibration isolators. In [32,33], the concept of using two pairs of inclined springs was presented, and attention was subsequently devoted by the scientific community on how to exploit it to further improve the performance of vibration isolators [34]. To this end, isolators adopting two pairs [35] and three pairs [36,37] of inclined springs have been proposed, and the target was to enlarge the isolation region. The configuration with two pairs of oblique springs was also effectively adopted to improve the performance of electro-magnetic vibration energy harvesters in [38], by exploiting the tri-stable characteristic [39]. Chaotic motion was also investigated to occur in isolators with two pairs of inclined springs [40], exhibiting a bi-stable characteristic. Springs configured to achieve a bi-stable characteristic have also been investigated in [41-44]. Springs arrangements, exhibiting geometrical nonlinearity, have been exploited to allow effective vibration isolation in all six degrees of freedom in space [45].

Most of the above cited works [9,10,12,15,16,21,23-27,29-31,34-37], were mainly focused on the realization of quasi-zero stiffness force–deflection curves. This characteristic is useful to achieve a high-static and low-dynamic stiffness behaviour, which simultaneously copes with two competing requirements in vibration isolation, i.e., carrying a payload with a low static deformation and exhibiting a low natural frequency to enlarge the isolation region. This is particularly helpful in protecting machines from resonance effects [46].

Other studies focused on achieving a softening-hardening stiffness nonlinearity using one pair of asymmetrically inclined springs [47], a tri-stable nonlinear characteristic using two pairs of symmetric springs [38], softening-zero-hardening stiffness characteristics [32,33,48], sigmoidal-shaped force–displacement curves [49], and even tailored [50] and adjustable [6,7] stiffness characteristics. A novel elastic metamaterial beam incorporating an X-shaped mechanism with springs, has also been proposed to improve the adjustability of the band-gap properties, where the nonlinear mechanism is able to mitigate or amplify the stiffness of the linear spring by parametrical design [51].

By focusing on geometrical combinations of springs only, and to better visualise the correspondence between the spring configuration and the related qualitative shape of the force–displacement curve, Fig. 1 illustrates three different cases where linear springs are combined in parallel to achieve different characteristics. In Fig. 1, f is the elastic restoring force, y is the imposed displacement of the suspended mass, and k is the spring stiffness, assumed equal for all the springs. In Fig. 1(a), a classical linear system is depicted, and the qualitative shape of the non-dimensional force–displacement curve is illustrated underneath the corresponding mechanical configuration. In terms of non-dimensional key-parameters, there is no parameter left for design purpose, and this is because after normalization (i.e., dividing by k and by a convenient parameter length) the non-dimensional force–displacement relationship can be rewritten simply as $\widehat{f} = \widehat{y}$. In Fig. 1(b), the classical quasi-zero stiffness configuration is depicted. With reference to the mechanical configuration and the indicated dimensional parameters, depending on the ratio of the free length of the spring, h_0, to the assembly distance, b, several qualitative shapes of the force–deflection curve, can be obtained, i.e., hardening, quasi-zero stiffness and bi-stable [7]. This configuration thus has one non-dimensional key-parameter for design, i.e., h_0/b. Fig. 1(c) depicts the spring configuration of

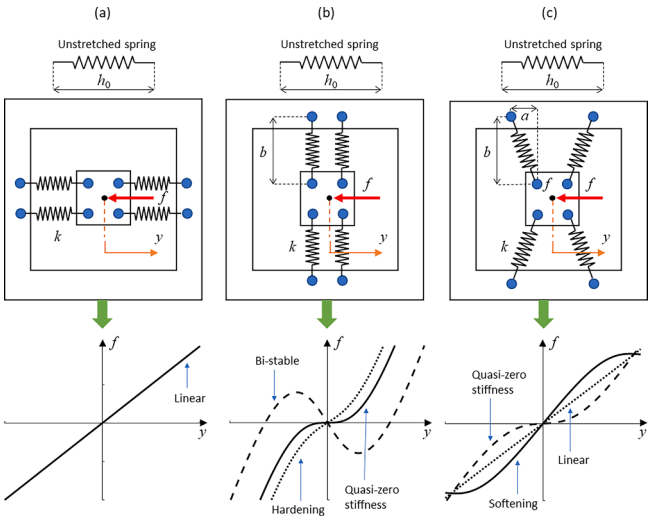

Fig. 1. Different mechanical configurations (top panels) at equilibrium using linear springs in parallel and (a) aligned, (b) orthogonal, or (c) inclined, respect to the direction of motion. Corresponding qualitative shapes of the force–deflection curves (bottom panels) that can be achieved, depending on the values of the related design parameters.

interest in this work, and previously discussed in [32]. In this case, there are two non-dimensional key-parameters useful for design, and they can be given, for example, by the ratio b/a and the ratio h_0/a, where a is a distance at the equilibrium condition, as shown in Fig. 1(c). Depending on the combination of such two design parameters, a softening-hardening, quasi-zero stiffness, and quasi-linear behaviour for large displacements can be achieved.

Other ways to introduce nonlinearity on purpose into dynamical systems is by nonlinear damping elements [5]. In vibration isolation problem, linear damping can usefully suppress the vibration peak at resonance, but can be detrimental at high frequencies due to an increase of the transmissibility. The main reason why the beneficial effects of nonlinear damping have been investigated in recent years is to reduce the transmissibility at higher frequencies. Nonlinear damping can be introduced and modelled as velocity dependent (e.g., cubic damping) or displacement dependent (i.e., resulting from geometrical configurations) [52].

In some of the studies dealing with the vibration performance of the above-mentioned nonlinear oscillators (which exploit different combinations of linkages reacting on springs to achieve nonlinear stiffness), damping has been simply modelled as a translational linear viscous element [9,11-13,24,25,53], accounting for different sources of friction. This assumption is valid when the amplitude of oscillation is relatively small, so that an equivalent linear viscous damping term can be considered. In other studies, due to the presence of hinges in the coupling linkages, both translational and rotational linear viscous damping effects have been considered [6,10,15-19,21-23,26-28]. In this latter case, the rotational components give rise to geometrical nonlinear damping effects along the translational direction of motion.

In the most recent works that considered geometrical combination of linear spring pairs only (i.e., without the presence of a specific underlying mechanical linkage), a linear viscous damping model has been considered [32-38,40]. Although those very recent works were mainly focussed on achieving and exploiting a nonlinear stiffness behaviour, modelling the dissipative effect of such strongly nonlinear systems as an equivalent linear viscous damper, could be an unrealistic assumption when high amplitude oscillation are considered. An attempt to consider inclined linear viscous damping leading to geometrical nonlinear damping has been reported in [47,52].

On the one hand, viscous damping may result in a reasonable assumption for hydraulic and pneumatic systems [54,55]. In particular, in [54] a novel bio-inspired hydraulic damper mimicking the behaviour found in abalone shells and bones have been proposed, leading to a relatively complex piece-wise damping model. In [55], a hydro-pneumatic quasi-zero stiffness vibration isolator is proposed, where quadratic damping and Coulomb dry friction have been considered.

On the other hand, viscous damping does not necessarily find a sufficient physical explanation when steel helical springs and articulated linkages are adopted. In fact, due to a mechanical implementation of a prototype device with joints and mating components in contact, dry friction is inevitable and comes along with other effects, classically modelled as viscous friction phenomena. Depending on the mechanical implementation, dry friction can be the dominant factor, especially when constant lubrication is not guaranteed, and this is particularly true in quasi-zero stiffness devices, where the elastic restoring component of the force is dramatically reduced, even causing friction-locking effects [56,57].

Some attempts to model dry friction in nonlinear oscillators consisting of linkages and/or springs can be found in [58] and [59], where the authors present models of a quasi-zero stiffness isolator which consider linear viscous damping and Coulomb dry friction. However, in [59] the authors did not report experimental observation. In [58], static and dynamic tests have been performed, and a constant dry friction coefficient was estimated. In [55], the authors did not report dynamic tests, and the experimental static stiffness curve did not manifest any clear dry friction hysteresis. A more comprehensive attempt to model high order displacement and velocity dependency in a friction model is reported in [60], where the authors adopt a nonlinear systems identification technique to estimate

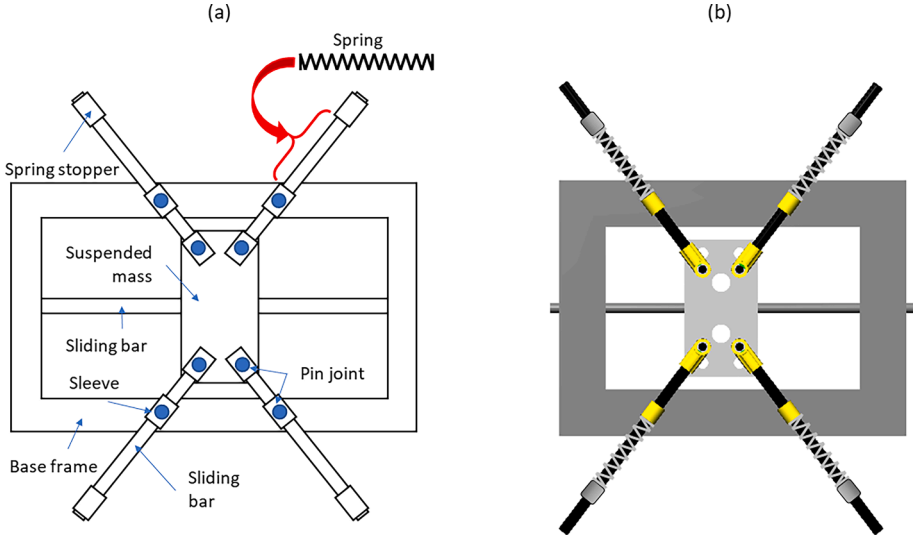

Fig. 2. (a) Schematic and (b) virtual model of the proposed mechanical oscillator suspension.

the damping and friction parameters in a prototype device of a bi-stable oscillator. Recent experimental works on how Coulomb friction affects the response of a linear oscillator have been reported in [61,62].

In the recent literature, there has not been a clear attempt to exploit a strong geometrical nonlinear stiffness configuration to realise a constant stiffness behaviour, leading to a linear system. Also, recent works on the investigation of nonlinear oscillators using pairs of inclined springs have not fully considered dry friction in their models nor showed the possibility to realise a linear elastic behaviour.

This paper thus fills this gap in the literature by investigating the static and dynamic behaviour of an oscillator with two pairs of inclined springs, delivering the following main contributions: (i) exploring the theoretical conditions for such a nonlinear oscillator to exhibit a quasi-linear force–displacement characteristic for large displacements, and (ii) modelling the effect of nonlinear friction in an X-shaped-spring prototype device.

In particular, the first issue represents a change of paradigm in the design of nonlinear oscillators, while the second issue advances the knowledge on the effect of a practical implementation of the theoretical model. The theoretical findings have been validated by experimental results.

Potential applications are foreseen in vibration energy harvesters [63,64], vibration isolators [65,66] and vibration absorbers [67,68], where having a linear elastic element is of interest and a nonlinear damping can be beneficial.

2. Static model of the oscillator

2.1. Dimensional parameters

A sketch and a virtual model of the proposed oscillator are illustrated in Fig. 2(a) and 2(b), respectively. For a reasonable mechanical implementation, several technological auxiliary components are considered, which play an important role in the static and dynamic performance of the device. A kinematic structure is considered to accommodate the required motion along the horizontal direction and avoid undesired motion and instabilities. This consists of a series of sliding bars, translational joints (sleeves) and rotational joints (pins), which form a one degree-of-freedom mechanism, but conversely introduce contact and friction among the several components. Four equal compression linear springs are adopted and mounted as indicated in Fig. 2. Depending on the free length of the springs and the position of the corresponding stoppers, a different level of initial compression can be achieved, which is assumed equal for the four springs.

Fig. 3 shows some more details of the proposed device. In particular, Fig. 3(a) shows the unloaded configuration, and Fig. 3(b) shows the loaded configuration, subject to the effect of an external static force, f_e, applied to the suspended mass.

The suspension system consists of four linear springs of stiffness k, connected to a rectangular support structure (the base frame) through joints. In the unloaded configuration of Fig. 3(a), the system is symmetric. The characteristic dimensions (evaluated in the unloaded equilibrium condition) are the constant lengths a and b, as labelled in Fig. 3(a), which determine the degree of inclination of the springs at static equilibrium, while $l_0 = \sqrt{a^2 + b^2}$ is the corresponding pin-pin distance. It is worth noting that the pin-pin distance varies during motion, as one pin is fixed to the oscillating mass, and the other pin is fixed to the sleeve (i.e., to a prismatic joint) on the frame. Thus, when the oscillating mass moves, the four bars slide inside their corresponding sleeves, making the pin-pin distance shorter or longer respect to the one at the static equilibrium. This is shown in the schematic of Fig. 3(b), where $l_1 < l_0 < l_2$. The parameter h represents the assembly length of the springs, and h_0 represents their free length. Since compression springs are adopted, the length of the springs during working conditions should not become greater than the free length of the springs, h_0 (this poses some

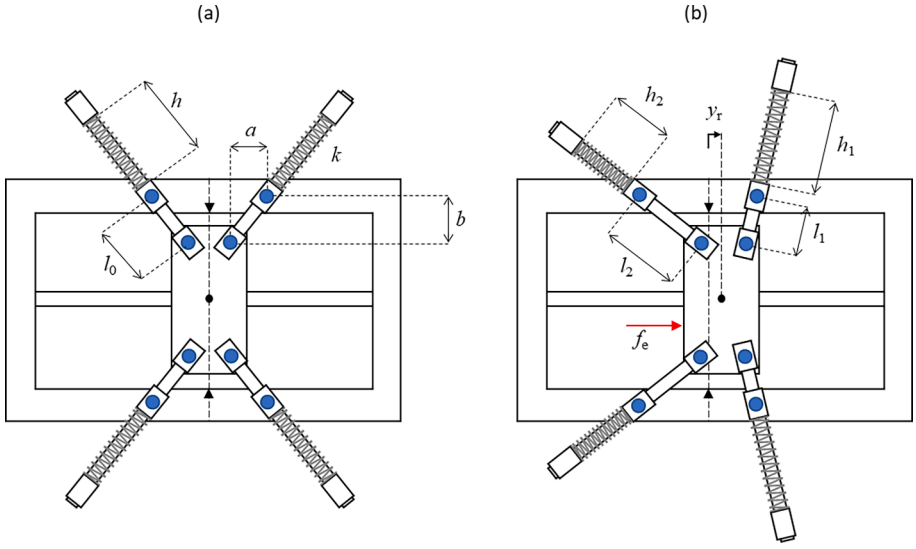

Fig. 3. Parameters of the proposed suspension in the (a) unloaded and (b) loaded configuration.

practical constraints, which are not usually considered in purely theoretical studies). When the suspended mass moves by a displacement y_r, with respect to the unloaded equilibrium condition, the configuration is that depicted in Fig. 3(b). On the right side of the oscillator, the springs are relaxed and assume the length indicated as h_1. Correspondingly, the pin-pin distance reduces and assumes the length indicated as $l_1 < l_0$. On the left side of the oscillator, the springs are compressed and assume the length indicated as h_2. Correspondingly, the pin-pin distance increases and assumes the length indicated as $l_2 > l_0$. In the configuration illustrated in Fig. 3(b), is thus $h_2 < h < h_1$.

2.2. Non-dimensional parameters and force–displacement curve

The static force–displacement characteristic of the suspension represented in Fig. 3 is given by the sum of two components, i.e., the contribution of the spring pair on the left and that on the right, yielding the following expression of the external force, f_e (opposite to the elastic force), as a function of the displacement, y_r, in terms of the system parameters

$$f_e = 2k\frac{(h_1 - h_0)(a - y_r)}{l_1} - 2k\frac{(h_2 - h_0)(a + y_r)}{l_2} \tag{1}$$

where

$$l_1 = \sqrt{(a - y_r)^2 + b^2} \tag{2}$$

$$l_2 = \sqrt{(a + y_r)^2 + b^2} \tag{3}$$

$$h_1 = h + l_0 - l_1 \tag{4}$$

$$h_2 = h + l_0 - l_2 \tag{5}$$

and l_0 and h have been defined above.

By then defining the spring compression factor as $\sigma = h_0/h$, Eq.(1) can be rewritten as

$$f_e = 2k\left[\frac{a - y_r}{\sqrt{(a - y_r)^2 + b^2}}\left(h(1-\sigma) + \sqrt{a^2 + b^2} - \sqrt{(a - y_r)^2 + b^2}\right) - \frac{a + y_r}{\sqrt{(a + y_r)^2 + b^2}}\left(h(1-\sigma) + \sqrt{a^2 + b^2} - \sqrt{(a + y_r)^2 + b^2}\right)\right] \tag{6}$$

The effects of the parameters of an X-shaped-spring suspension on the shape of the force–displacement curve has been extensively reported in [69]. In this paper, focus is particularly devoted to the achievement of a quasi-linear behaviour for large displacements.

Examining Eq. (6), it is clear that for $h(1-\sigma) + \sqrt{a^2 + b^2} = 0$, it reduces to the following linear relationship

$$f_e = 2k[-(a - y_r) + (a + y_r)] = 4ky_r \tag{7}$$

This can also be better investigated by expanding Eq. (6) in Taylor series as

$$f_e \approx k_1 y_r + k_3 {y_r}^3 + k_5 {y_r}^5 + k_7 {y_r}^7 + \cdots \tag{8}$$

where

$$k_1 = k\frac{4\left(a^2\sqrt{a^2 + b^2} - h(1-\sigma)b^2\right)}{\left(a^2 + b^2\right)^{3/2}} \tag{9}$$

$$k_3 = k\frac{2b^2\left(b^2 - 4a^2\right)\left(h(1-\sigma) + \sqrt{a^2 + b^2}\right)}{\left(a^2 + b^2\right)^{7/2}} \tag{10}$$

$$k_5 = k\frac{3b^2\left(8a^4 - 12a^2b^2 + b^4\right)\left(h(1-\sigma) + \sqrt{a^2 + b^2}\right)}{2\left(a^2 + b^2\right)^{11/2}} \tag{11}$$

$$k_7 = k\frac{b^2\left(-64a^6 + 240a^4b^2 - 120a^2b^4 + 5b^6\right)\left(h(1-\sigma) + \sqrt{a^2 + b^2}\right)}{4\left(a^2 + b^2\right)^{15/2}} \tag{12}$$

It can be thus easily seen also from Eqs. (10–12) that the higher-order terms (except the first one reported in Eq. (9)) go to zero when the relationship $h(1-\sigma)+\sqrt{a^2+b^2}=0$ is satisfied. This condition can be rewritten by emphasizing the spring compression factor needed to realize a linear force–displacement characteristic for large displacements, as

$$\sigma_{\text{lin}} = 1+\frac{\sqrt{a^2+b^2}}{h} \tag{13}$$

It is interesting to note, also, that both spring pairs on the left and right side of the suspension behave in a linear fashion as well, as highlighted in Eq. (7). In particular, the spring pair on the right presents a force–displacement characteristic of $-2k(a-y_r)$ and the spring pair on the left presents a force–displacement characteristic of $2k(a+y_r)$. So, it is not the combination of the two pairs of springs that determines the sought behaviour, rather it is the free length parameter of each pair, which determines a linear behaviour for both pairs of springs.

Equation (13), i.e., the requirement for a linear behaviour of the nonlinear oscillator, is plotted in Fig. 4 as a function of the non-dimensional parameter h/a for different values of the other non-dimensional parameter b/a. To better visualize the trend of σ_{lin} for relatively lower and higher values of h/a, a logarithmic scale has been adopted for the horizontal axis. It can be seen that as the normalized assembled length of the spring, h/a, decreases, the value of σ_{lin} increases. When the value of h/a becomes less than 1, the free length of the spring, h_0, can become more than twice the assembled length, h. For increasing values of h/a, then σ_{lin} tends to 1 meaning that the springs are assembled neither in tension nor in compression, so that $h = h_0$.

To show how the spring compression factor affects the linear behaviour of the force–displacement curve for large displacements, the non-dimensional force, f_e/ak, is plotted in Fig. 5(a-d) as a function of the non-dimensional displacement, y_r/a, for different values of b/a, h/a, and in each case for three values of σ, equal to 0.5, 1 and 2 times the corresponding value of σ_{lin}.

From Fig. 5(a,b) it can be seen that, for lower values of the ratio b/a, a relatively large variation of the value of σ respect to σ_{lin} has a large effect on the linear trend of the force deflection curve for large displacements. For $b/a = 1$, as in Fig. 5(c,d) the deviation from a linear trend is less evident, and the effect of σ is mainly to change the quasi-linear stiffness of the curve.

3. Static test on a prototype device

To validate the theoretical results obtained in the previous section, a prototype device was built and assembled, and shown in Fig. 6 (a). The suspended mass was made of steel, and the support structure (the base frame) was made of aluminum (black-anodised on the surface). The bars, bushings, and connectors were lightweight plastic LEGO® components. Compression springs were off-the-shelf purchased components and their stiffness have been measured independently. The reflective markers in Fig. 6(a) were used to measure the displacement by laser sensors, as will be described in the following sections. The system parameters are listed in Table 1.

The static characteristic of the prototype device was measured using the setup shown in Fig. 6(b). The support frame was fixed on the top of an optical table. One extreme of a long wire was attached to the suspended mass. The wire was then wrapped around a pulley at the edge of the optical table and its other end was attached to a weight container. The change in displacement, y_r, of the suspended mass due to a change in the weight pulling the wire, was measured by a laser triangulator pointing at the corresponding reflective marker. Loading and unloading tests were performed, and results are reported in Fig. 7, in the form of a force–displacement graph. In Fig. 7, the experimental data are denoted by square markers.

A clear hysteretic cycle is evident in the test results of Fig. 7. However, respect to a classical dry (Coulomb) friction model, i.e., $f_\mu =$

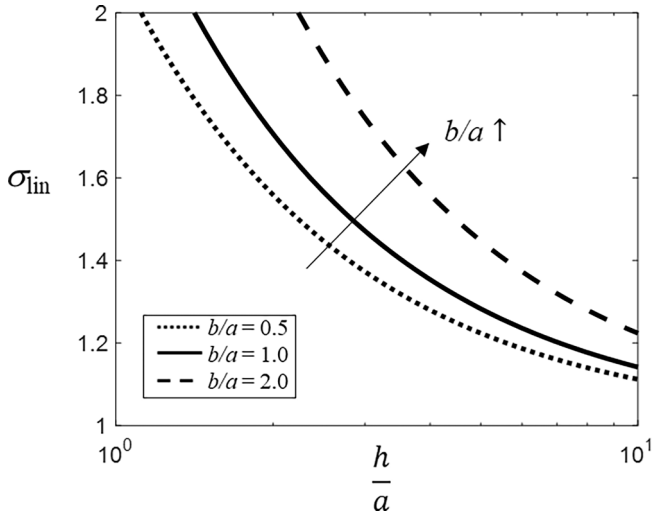

Fig. 4. Spring compression factor to realise a linear force–displacement curve for large displacements, as a function of h/a, and for different values of b/a.

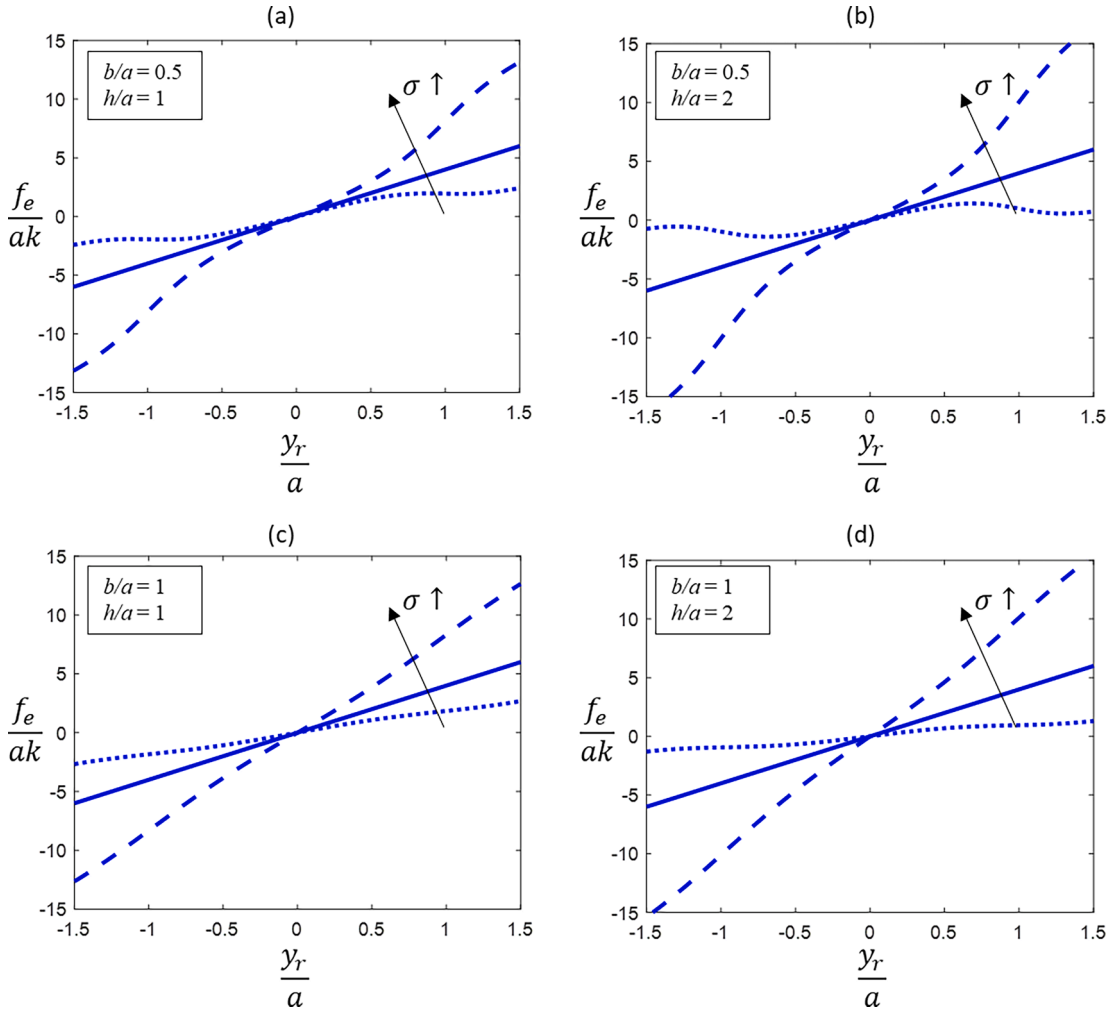

Fig. 5. Non-dimensional force–displacement curve for three values of σ corresponding to $0.5\sigma_{\text{lin}}, \sigma_{\text{lin}}, 2\sigma_{\text{lin}}$, and different combinations of the non-dimensional parameters b/a and h/a as labelled.

$\mu_0 sign\left(\dot{y}_r\right)$, a nonlinear dependency on the amplitude of motion manifests.

To reflect this, perhaps one of the simplest models that can be considered is one where the friction force coefficient is assumed not to be constant, rather varying with the relative displacement amplitude in a polynomial way of the following form

$$f_\mu = \left(\mu_0 + \mu_2 y_r^2 + \mu_4 y_r^4 + \mu_6 y_r^6 + \ldots\right) sign\left(\dot{y}_r\right) \tag{14}$$

where the overdot denotes derivation respect to time. This form could then be obtainable from a Taylor series expansion of a more complex analytical model, similarly to what was done for the elastic force in Eq. (8). In fact, it is speculated that the dependency of the dry friction parameter on the amplitude displacement is due to the inherently nonlinear architecture of the mechanisms. Due to the presence of the inclined linkages (accommodating the springs), the higher the displacement the higher the reaction force on the joints, and consequently the higher the contact force in the couplings.

For the specific prototype under test, it resulted that the constant and quadratic terms were enough to fit the experimental data. The results of the fitting are plotted in Fig. 7 as a thick dashed curve, while the thick solid curve represents the elastic force, f_e, which it is obtained from Eq. (6), using the parameters listed in Table 1. The thick dotted line will be described in the next section.

From Fig. 7, it can be thus noted that the backbone curve of the hysteretic cycle has a quasi-linear trend for large displacements, and that the prototype device is characterized by a large dry friction force, whose parameter is however modelled by an amplitude-dependent relationship in terms of the displacement. For the static test results of Fig. 7, the following parameters were estimated by fitting the experimental data, $\mu_0 = 0.45$ N and $\mu_2 = 3000$ N/m^2.

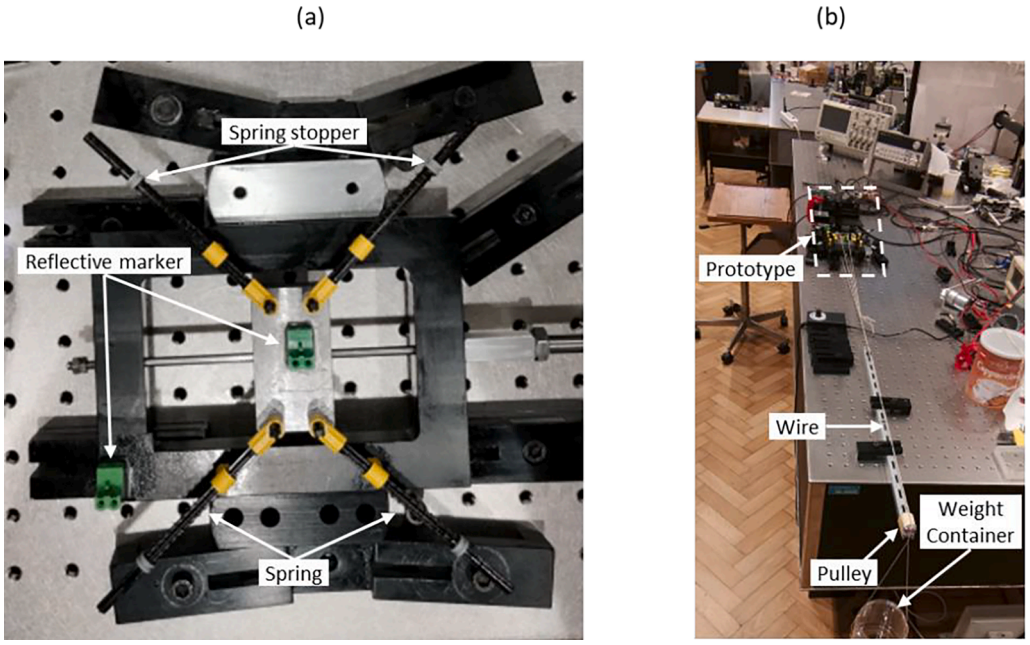

Fig. 6. (a) Prototype device of the model in Fig. 2 and (b) setup for static test.

Table 1
Parameters of the prototype oscillator used in the static model.

a (mm)	b (mm)	h (mm)	h_0 (mm)	k (N/m)
21	21	38	51	110

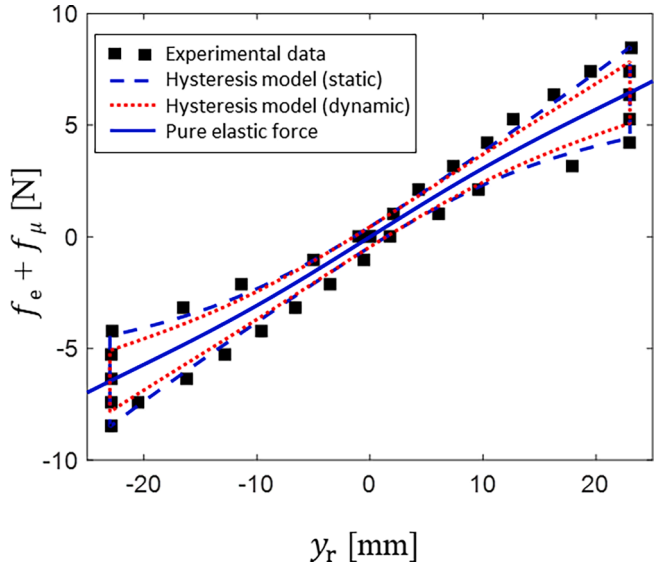

Fig. 7. Results of the experimental static test. The vertical axis denotes the sum of the elastic force and the friction force.

4. Dynamic model of the oscillator

To generalise the dynamic analysis, an equivalent model of the X-shaped-spring oscillator is illustrated in Fig. 8, where an equivalent spring force, given by Eq. (6), and an equivalent dry friction force, given by Eq. (14), have been indicated. Also, an

equivalent form of viscous friction is assumed and added to the model. In the dynamic model, the oscillating mass is denoted by m and the base frame is supposed to be excited by an imposed harmonic displacement $y_b = Y_b\cos(\omega t)$, where Y_b is the displacement amplitude, ω is the circular frequency, t is time, and y_r, as indicated in Fig. 8, now denotes the relative displacement between the suspended mass and the base frame.

For dynamic purposes, the equation of motion of the oscillator depicted in Fig. 8 is conveniently rewritten below as

$$m\ddot{y}_r + \widetilde{c}(y_r)\dot{y}_r + \widetilde{\mu}(y_r)\mathrm{sign}\left(\dot{y}_r\right) + \widetilde{k}(y_r)y_r = -m\ddot{y}_b \tag{15}$$

where amplitude-dependent coefficients have been assumed for viscous friction, dry friction, and stiffness, respectively, as

$$\widetilde{c}(y_r) = c_0 + c_2 {y_r}^2 + c_4 {y_r}^4 + c_6 {y_r}^6 \tag{16}$$

$$\widetilde{\mu}(y_r) = \mu_0 + \mu_2 {y_r}^2 + \mu_4 {y_r}^4 + \mu_6 {y_r}^6 \tag{17}$$

$$\widetilde{k}(y_r) = k_0 + k_2 {y_r}^2 + k_4 {y_r}^4 + k_6 {y_r}^6 \tag{18}$$

It is noted that the expression of the elastic term in Eq. (15) has also been approximated by a polynomial expansion in Eq. (18) to derive a closed-form analytical solution to the equation of motion.

Moreover, it is noted how the assumption made on the friction model in Eq. (14) let one derive equivalent and more elegant formulations of the expressions in Eqs. (16–18).

To reduce the number of design parameters in the analysis, non-dimensional variables are defined as follows: $\omega_0 = \sqrt{k_0/m}$ is the linearised natural frequency, $\widehat{\omega} = \omega/\omega_0$ is the normalised circular frequency, $\widehat{t} = \omega_0 t$ is the normalised time, $\zeta = c_0/2m\omega_0$ is the normalised viscous friction coefficient, $\widehat{y}_r = y_r/a$ is the normalized relative displacement, $\widehat{Y}_b = Y_b/a$ is the normalized base displacement amplitude, $\mu = \mu_0/ak_0$ is the normalised dry friction coefficient, and the following normalized equation of motion is obtained

$$\widehat{y}_r'' + 2\zeta\widehat{c}(\widehat{y}_r)\widehat{y}_r' + \mu\widehat{\mu}(\widehat{y}_r)\mathrm{sign}(\widehat{y}_r') + \widehat{k}(\widehat{y}_r)\widehat{y}_r = \widehat{\omega}^2\widehat{Y}_b\cos(\widehat{\omega}\tau) \tag{19}$$

where

$$\widehat{c}(\widehat{y}_r) = 1 + \frac{c_2}{c_0}a^2{\widehat{y}_r}^2 + \frac{c_4}{c_0}a^4{\widehat{y}_r}^4 + \frac{c_6}{c_0}a^6{\widehat{y}_r}^6 = 1 + \widehat{c}_2{\widehat{y}_r}^2 + \widehat{c}_4{\widehat{y}_r}^4 + \widehat{c}_6{\widehat{y}_r}^6 \tag{20}$$

$$\widehat{\mu}(\widehat{y}_r) = 1 + \frac{\mu_2}{\mu_0}a^2{\widehat{y}_r}^2 + \frac{\mu_4}{\mu_0}a^4{\widehat{y}_r}^4 + \frac{\mu_6}{\mu_0}a^6{\widehat{y}_r}^6 = 1 + \widehat{\mu}_2{\widehat{y}_r}^2 + \widehat{\mu}_4{\widehat{y}_r}^4 + \widehat{\mu}_6{\widehat{y}_r}^6 \tag{21}$$

$$\widehat{k}(\widehat{y}_r) = 1 + \frac{k_2}{k_0}a^2{\widehat{y}_r}^2 + \frac{k_4}{k_0}a^4{\widehat{y}_r}^4 + \frac{k_6}{k_0}a^6{\widehat{y}_r}^6 = 1 + \widehat{k}_2{\widehat{y}_r}^2 + \widehat{k}_4{\widehat{y}_r}^4 + \widehat{k}_6{\widehat{y}_r}^6 \tag{22}$$

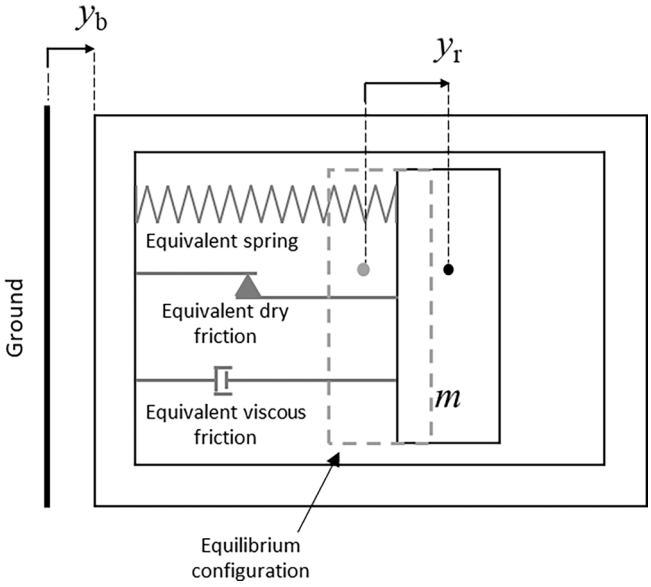

Fig. 8. Equivalent model of the X-shaped-spring oscillator.

and the normalized coefficients of the viscous friction, dry friction and stiffness have been introduced in the rightest side of Eq. (20), Eq. (21) and Eq. (22), respectively, with a hat.

It is then assumed a solution to the equation of motion which is predominately harmonic in terms of displacement, i.e. $\hat{y}_r = \hat{Y}_r(\hat{t})\cos(\hat{\omega}\hat{t}+\varphi(\hat{t}))$, and velocity, i.e., $\hat{y}_r{}'(\hat{t}) = -\hat{\omega}\hat{Y}_r(\hat{t})\sin(\hat{\omega}\hat{t}+\varphi(\hat{t}))$, where φ is the phase between the relative displacement and the base displacement.

The assumptions on harmonic response imply that

$$\hat{Y}_r{}'\cos(\hat{\omega}\hat{t}+\varphi) - \hat{Y}_r\sin(\hat{\omega}\hat{t}+\varphi)\varphi' = 0 \tag{23}$$

where the explicit dependency of $\hat{Y}_r$ and φ on time $\hat{t}$, has been dropped for convenience. By then substituting the expression of the assumed harmonic response into the equation of motion, Eq. (19), the following normalised equation of motion is obtained

$$\begin{aligned}&\hat{Y}_r'\hat{\omega}\sin(\hat{\omega}\hat{t}+\varphi) + \hat{Y}_r\hat{\omega}\cos(\hat{\omega}\hat{t}+\varphi)(\hat{\omega}+\varphi') + 2\zeta\hat{c}(\hat{y}_r)\hat{Y}_r\hat{\omega}\sin(\hat{\omega}\hat{t}+\varphi) + \mu\hat{\mu}(\hat{y}_r)\mathrm{sign}(\hat{Y}_r\hat{\omega}\sin(\hat{\omega}\hat{t}\\ &+\varphi)) - \hat{k}(\hat{y}_r)\hat{Y}_r\cos(\hat{\omega}\hat{t}+\varphi) + \hat{\omega}^2\hat{Y}_b\cos(\hat{\omega}\hat{t})\\ &=0\end{aligned} \tag{24}$$

Solving Eq. (23) and Eq. (24) in terms of $\hat{Y}_r{}'$ and φ', and taking into account Eqs. (20)–(22), yields

$$\begin{aligned}\hat{Y}_r' = &-\frac{1}{\hat{\omega}}\sin(\hat{\omega}\hat{t}+\varphi)\big(-\hat{Y}_r\cos(\hat{\omega}\hat{t}+\varphi)\big((1-\hat{\omega}^2) + \hat{k}_2\hat{Y}_r{}^2\cos^2(\hat{\omega}\hat{t}+\varphi) + \hat{k}_4\hat{Y}_r{}^4\cos^4(\hat{\omega}\hat{t}+\varphi) + \hat{k}_6\hat{Y}_r{}^6\cos^6(\hat{\omega}\hat{t}+\varphi)\big) + \mu\big(1\\ &+\hat{\mu}_2\hat{Y}_r{}^2\cos^2(\hat{\omega}\hat{t}+\varphi) + \hat{\mu}_4\hat{Y}_r{}^4\cos^4(\hat{\omega}\hat{t}+\varphi) + \hat{\mu}_6\hat{Y}_r{}^6\cos^6(\hat{\omega}\hat{t}+\varphi)\big)\mathrm{sign}(\hat{Y}_r\hat{\omega}\sin(\hat{\omega}\hat{t}+\varphi)) + 2\zeta\hat{\omega}\hat{Y}_r\sin(\hat{\omega}\hat{t}+\varphi)\big(1\\ &+\hat{c}_2\hat{Y}_r{}^2\cos^2(\hat{\omega}\hat{t}+\varphi) + \hat{c}_4\hat{Y}_r{}^4\cos^4(\hat{\omega}\hat{t}+\varphi) + \hat{c}_6\hat{Y}_r{}^6\cos^6(\hat{\omega}\hat{t}+\varphi)\big) + \hat{\omega}^2\hat{Y}_b\cos(\hat{\omega}\hat{t})\big)\end{aligned} \tag{25}$$

$$\begin{aligned}\varphi' = &-\frac{1}{\hat{Y}_r\hat{\omega}}\cos(\hat{\omega}\hat{t}+\varphi)\big(-\hat{Y}_r\cos(\hat{\omega}\hat{t}+\varphi)\big((1-\hat{\omega}^2) + \hat{k}_2\hat{Y}_r{}^2\cos^2(\hat{\omega}\hat{t}+\varphi) + \hat{k}_4\hat{Y}_r{}^4\cos^4(\hat{\omega}\hat{t}+\varphi) + \hat{k}_6\hat{Y}_r{}^6\cos^6(\hat{\omega}\hat{t}+\varphi)\big) + \mu\big(1\\ &+\hat{\mu}_2\hat{Y}_r{}^2\cos^2(\hat{\omega}\hat{t}+\varphi) + \hat{\mu}_4\hat{Y}_r{}^4\cos^4(\hat{\omega}\hat{t}+\varphi) + \hat{\mu}_6\hat{Y}_r{}^6\cos^6(\hat{\omega}\hat{t}+\varphi)\big)\mathrm{sign}(\hat{Y}_r\hat{\omega}\sin(\hat{\omega}\hat{t}+\varphi)) + 2\zeta\hat{\omega}\hat{Y}_r\sin(\hat{\omega}\hat{t}\\ &+\varphi)\big(1+\hat{c}_2\hat{Y}_r{}^2\cos^2(\hat{\omega}\hat{t}+\varphi) + \hat{c}_4\hat{Y}_r{}^4\cos^4(\hat{\omega}\hat{t}+\varphi) + \hat{c}_6\hat{Y}_r{}^6\cos^6(\hat{\omega}\hat{t}+\varphi)\big) + \hat{\omega}^2\hat{Y}_b\cos(\hat{\omega}\hat{t})\big)\end{aligned} \tag{26}$$

The variables $\hat{Y}_r'$ and φ' are assumed to vary slowly in time, so that their averages are assumed to be constant over a time period $2\pi/\hat{\omega}$. Integrating Eqs. (25) and (26) over such a time period gives, respectively,

$$2\hat{\omega}\hat{Y}_r' = -\frac{4\mu}{\pi}\left(1+\frac{1}{3}\hat{\mu}_2\hat{Y}_r{}^2+\frac{1}{5}\hat{\mu}_4\hat{Y}_r{}^4+\frac{1}{7}\hat{\mu}_6\hat{Y}_r{}^6\right) - 2\zeta\hat{\omega}\hat{Y}_r\left(1+\frac{1}{4}\hat{c}_2\hat{Y}_r{}^2+\frac{1}{8}\hat{c}_4\hat{Y}_r{}^4+\frac{5}{64}\hat{c}_6\hat{Y}_r{}^6\right) - \hat{\omega}^2\hat{Y}_b\sin(\varphi) \tag{27}$$

$$2\hat{Y}_r\hat{\omega}\varphi' = \hat{Y}_r+\frac{3}{4}\hat{k}_2\hat{Y}_r{}^3+\frac{5}{8}\hat{k}_4\hat{Y}_r{}^5+\frac{35}{64}\hat{k}_6\hat{Y}_r{}^7 - \hat{\omega}^2\hat{Y}_r - \hat{\omega}^2\hat{Y}_b\cos(\varphi) \tag{28}$$

For steady-state oscillation, without amplitude and phase variations, the left-hand sides of Eq. (27) and Eq. (28) are zero, which results in

$$\frac{4\mu}{\pi}M + 2\zeta C\,\hat{\omega}\hat{Y}_r = -\hat{\omega}^2 Y_b\sin(\varphi) \tag{29}$$

$$\hat{Y}_r\left(K-\hat{\omega}^2\right) = \hat{\omega}^2 Y_b\cos(\varphi) \tag{30}$$

where

$$C = 1+\frac{1}{4}\hat{c}_2\hat{Y}_r{}^2+\frac{1}{8}\hat{c}_4\hat{Y}_r{}^4+\frac{5}{64}\hat{c}_6\hat{Y}_r{}^6 \tag{31}$$

$$M = 1+\frac{1}{3}\hat{\mu}_2\hat{Y}_r{}^2+\frac{1}{5}\hat{\mu}_4\hat{Y}_r{}^4+\frac{1}{7}\hat{\mu}_6\hat{Y}_r{}^6 \tag{32}$$

$$K = 1+\frac{3}{4}\hat{k}_2\hat{Y}_r{}^2+\frac{5}{8}\hat{k}_4\hat{Y}_r{}^4+\frac{35}{64}\hat{k}_6\hat{Y}_r{}^6 \tag{33}$$

Squaring and adding Eq. (29) and Eq. (30), gives the following amplitude-frequency equation

$$\hat{\omega}^4\left(\hat{Y}_r{}^2-\hat{Y}_b{}^2\right)+2\hat{\omega}^2\hat{Y}_r{}^2\left(2\zeta^2C^2-K\right)+\frac{16\mu\zeta}{\pi}\hat{\omega}\hat{Y}_rCM+\hat{Y}_r{}^2K^2+\left(\frac{4\mu}{\pi}M\right)^2 = 0 \tag{34}$$

while dividing Eq. (29) by Eq. (30), gives the following expression for the phase

$$\tan(\varphi) = -\frac{\frac{4\mu}{\pi}M + 2\zeta\widehat{\omega}\widehat{Y}_r C}{\widehat{Y}_r(K - \widehat{\omega}^2)} \tag{35}$$

Equation (34) is the analytic expression of a quartic equation in terms of $\widehat{\omega}$, and can be thus numerically solved to plot the frequency response curve, for given combinations of the system parameters.

By defining the normalized absolute displacement of the suspended mass as $\widehat{y}_a = \widehat{y}_b + \widehat{y}_r = \widehat{Y}_a\cos(\widehat{\omega}\widehat{t} + \varphi_a)$, the absolute displacement transmissibility is determined as [70]

$$\frac{\widehat{Y}_a}{\widehat{Y}_b} = \sqrt{1 - \frac{\widehat{Y}_r^{\,2}}{\widehat{Y}_b^{\,2}} + \frac{2K}{\widehat{\omega}^2}\frac{\widehat{Y}_r^{\,2}}{\widehat{Y}_b^{\,2}}} \tag{36}$$

As the model formulated above accounts for the dry friction effect, a brake-loose frequency, $\widehat{\omega}_{bl}$, as discussed in [56], can be defined as the frequency below which no relative motion exists ($\widehat{Y}_r = 0$) between the oscillating mass and the base frame, and thus $\widehat{Y}_a = \widehat{Y}_b$.

An analytic expression of such frequency can be obtained by setting $\widehat{Y}_r = 0$ in Eq. (34), thus yielding

$$\widehat{\omega}_{bl} = 2\sqrt{\frac{\mu}{\pi\widehat{Y}_b}} \tag{37}$$

5. Dynamic tests on a prototype device

For dynamic validation, the prototype device described in Section 3 was incorporated into the experimental setup shown in Fig. 9.

The base frame of the oscillator was connected to the sliding rod of a crack-slider mechanism actuated by an electrical rotational motor. The crank length, r (with $Y_b = r$), was adaptable to 3, 4, and 5 mm, and the connecting rod length, d, was 50 mm. The ratio r/d is less or equal to 0.1, and the slider motion is thus considered to be predominantly harmonic at the constant rotational speed of the motor. Two laser triangulators were adopted for a contact-less, rapid and accurate measurement of the displacements of the moving components, i.e., the base frame and the oscillating mass. To this purpose, reflective and lightweight markers were attached to the base frame and the oscillating mass. A video showing the prototype device in working conditions is reported as a supplementary material in Appendix A.

For each value of the crank length, as reported above, dynamic experimental tests were performed. These consisted in driving the motor at different constant speeds for at least 5 s, and acquiring data in the next 2 s. Such procedure was adopted to let the transient decay away and thus measure the steady-state regime only.

It was verified that both recorded displacements were predominantly harmonic at the revolute frequency of the electrical motor, and higher/lower order harmonics were negligible.

For each of the three tests, the first Fourier coefficient of each single measured time history was extracted and plotted in Fig. 10(a-c) by a marker, as a function of the test frequency. Circle markers denote the displacement amplitude of the base frame, and square markers denote the displacement amplitude of the oscillating mass. The brake-loose frequency calculated by Eq. (37) is also indicated in Fig. 10.

The approximate analytical expression of the amplitude-frequency equation given in Eq. (34) is also plotted in Fig. 10(a-c) as a solid curve. The effective parameters used in the dynamic model are reported in Table 2 below.

Conversely, the following remaining parameters are all set to zero: μ_4, μ_6, c_0, c_2, c_4, c_6.

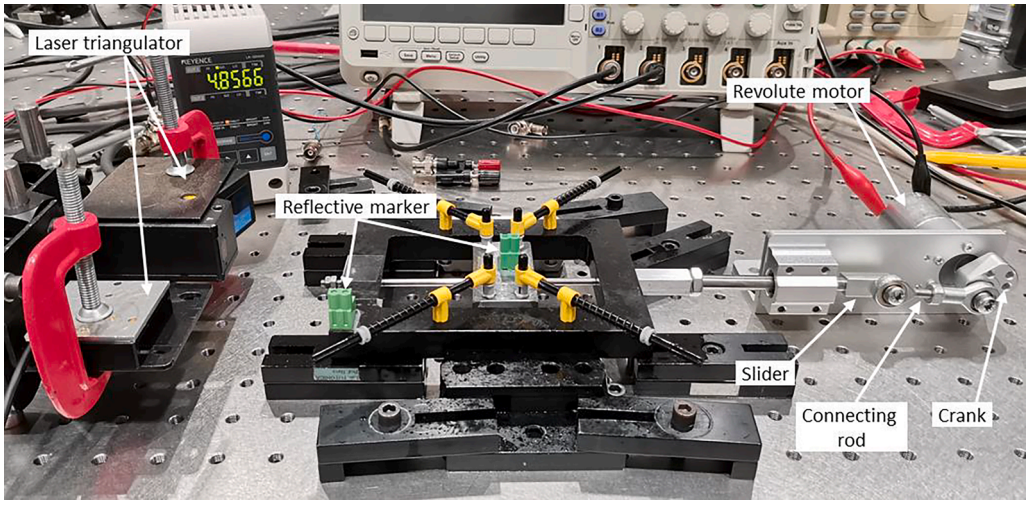

Fig. 9. Experimental setup for dynamic tests.

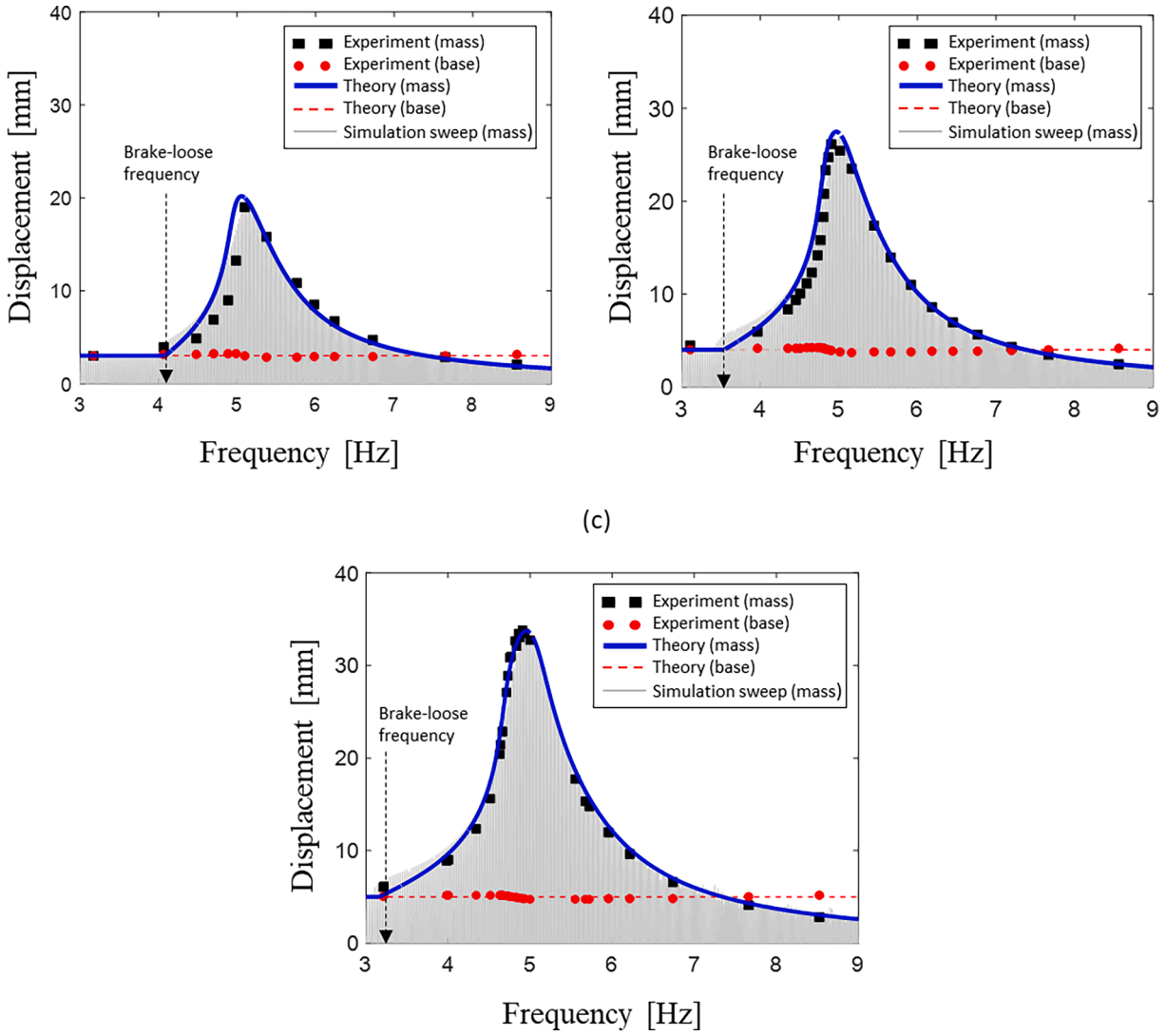

Fig. 10. Results of experimental dynamic tests, for (a) $Y_b = 3$ mm, (b) $Y_b = 4$ mm, (c) $Y_b = 5$ mm.

In fact, it was not necessary to account for any viscous damping in the system, as the considered dry friction was enough to fit the experimental data.

From Fig. 10, it can be seen that the theoretical model fits the experimental results relatively well, uncovering the real quasi-linear behaviour for large displacements of the prototype device. In particular, it is noted that the peak displacement amplitude was about 35 mm, which is larger than the characteristic dimension a of the oscillator, which was 21 mm. This shows that the oscillator is working in the (relatively) large-amplitude regime.

Furthermore, a reduction in the estimated value of quadratic dry friction coefficient, μ_2, was attained in the dynamic tests, with respect to the results of the static test reported in Fig. 7. It is speculated that such a reduction is due to the nature of the static test, which was affected by dry static friction, while a transition from dry static friction to dry dynamic friction was expected during motion.

When the friction coefficients in Table 2 are used in Eq. (14), the dotted line in Fig. 7 is obtained, and a slightly narrower hysteretic cycle is achieved.

To further validate these results, a slow sweep simulation is performed by direct numerical integration of the equation of motion in Eq. (15), and simulated results are also plotted in Fig. 10 (a-c) as a thin light grey line.

Table 2
Parameters of the prototype oscillator used in the dynamic model.

m (kg)	μ_0 (N)	μ_2 (N/m^2)	k_0 (N/m)	k_2 (N/m^3)	k_4 (N/m^5)	k_6 (N/m^7)
0.29	0.45	1750	318	$-1.2 \bullet 10^5$	$1.1 \bullet 10^8$	$-2.9 \bullet 10^{10}$

It is worth noting that the presence of the quadratic dry friction coefficient, μ_2, assures a bounded response of the oscillator at resonance. This is not necessarily granted when classical Coulomb friction model is assumed, and requires the assumption of a viscous friction coefficient to guarantee the expected bounded response [56].

To compare the results at the three different excitation levels (i.e., Y_b = 3, 4, and 5 mm), Fig. 11 shows the corresponding displacement transmissibility. In each case, the star marker denotes the brake-loose frequency, calculated using Eq. (37). It can be seen that the oscillator performs in a linear-like fashion, i.e., the peak transmissibility and its corresponding frequency are very slightly affected by the excitation level. The main difference among the three transmissibility curves is due to the different values of the brake-loose frequency, which decreases for increasing level of excitation amplitude, as evident from the relation between $\widehat{\omega}_{bl}$ and $\widehat{Y}_b$ in Eq. (37).

6. Insight on the identified dynamic model

Although viscous friction was modelled, experimental dynamic data were well-fitted by assuming a dry friction model only, having a constant and quadratic term (as a function of the relative displacement). The presence of this latter dry friction term was enough to assure a bounded response of the oscillator at resonance, with no need to estimate a viscous friction coefficient.

For such a case, considering $C = 0$, the amplitude-frequency relationship in Eq. (34) reduces to

$$\widehat{\omega}^4\left(\widehat{Y}_r^{\,2}-\widehat{Y}_b^{\,2}\right)-2\widehat{\omega}^2\widehat{Y}_r^{\,2}K+\widehat{Y}_r^{\,2}K^2+\left(\frac{4\mu}{\pi}M\right)^2=0 \tag{38}$$

which is a quadratic equation in terms of $\widehat{\omega}^2$, and can be thus easily solved analytically to plot the frequency response of the nonlinear oscillator.

For Eq. (38) it is also possible to determine a useful relationship for the stability of the steady-state response, which could be used for subsequent analysis. To a first-order approximation, this is given by considering the derivative of Eq. (38) respect to $\widehat{Y}_r$, setting it to zero and then solving for $\widehat{\omega}$ to give

$$\widehat{\omega}=\sqrt{K+\frac{1}{2}\left(\widehat{Y}_r\frac{\partial \mathrm{K}}{\partial \widehat{Y}_r}\pm\frac{\sqrt{-64\mu^2M\partial M\Big/\partial\widehat{Y}_r+\pi^2\widehat{Y}_r^{\,3}(\partial K/\partial\widehat{Y}_r)^2}}{\pi\sqrt{\widehat{Y}_r}}\right)} \tag{39}$$

where

$$\frac{\partial M}{\partial \widehat{Y}_r}=\frac{2}{3}\widehat{\mu}_2\widehat{Y}_r+\frac{4}{5}\widehat{\mu}_4\widehat{Y}_r^{\,3}+\frac{6}{7}\widehat{\mu}_6\widehat{Y}_r^{\,5} \tag{40}$$

$$\frac{\partial K}{\partial \widehat{Y}_r}=\frac{3}{2}\widehat{k}_2\widehat{Y}_r+\frac{5}{2}\widehat{k}_4\widehat{Y}_r^{\,3}+\frac{105}{32}\widehat{k}_6\widehat{Y}_r^{\,5} \tag{41}$$

To validate the proposed model and stability conditions over a more general nonlinear behaviour, the results of two simulation

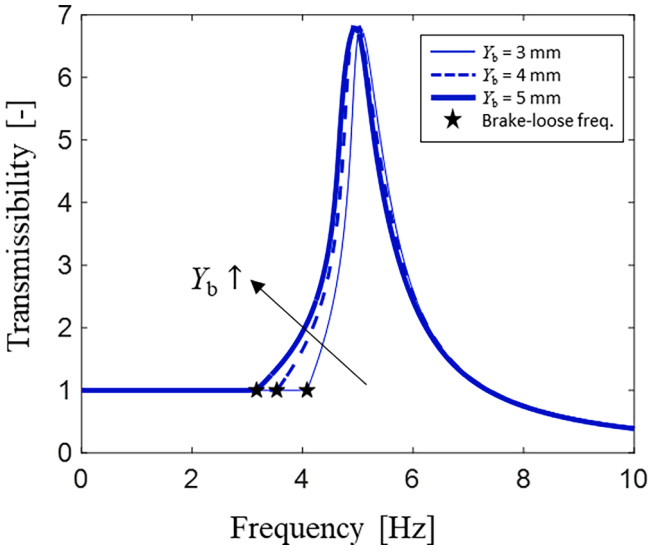

Fig. 11. Displacement transmissibility for the three different levels of excitation amplitude.

examples are reported in Figs. 12 and 13, for different combinations of the system parameters. These combinations of numerical values for the system parameters were arbitrarily selected to achieve a softening-hardening and a hardening–softening behaviour, respectively illustrated in Figs. 12 and 13. In particular, Fig. 12 considers the force–displacement curve previously shown in Fig. 5(a) with the dotted line, and Fig. 13 considers the force–displacement curve previously shown in Fig. 5(a) with the dashed line (note that, due to the definition of the linearised natural frequency $\omega_0 = \sqrt{k_0/m}$, a factor of k_0/k applies to the vertical axis of Fig. 12 and Fig. 13, respect to those in Fig. 5). The non-dimensional parameters used for the suspension dimensions are $\widehat{b} = b/a = 0.5$ and $\widehat{h} = h/a = 1$. In Fig. 12 and Fig. 13, panel (a) shows the force–displacement curve and the effect of friction, panel (b) shows the normalized amplitude dependent friction coefficient, panels (c) and (d) show the frequency response curves and the corresponding stability curves for two different values of excitation amplitude. Numerical simulation sweeps are also plotted for validation of the analytical model.

It can be seen that the approximate closed-form expression of the amplitude-frequency equation (Eq. (38)) compares well with the numerical results. The jump-up and jump-down frequencies are captured quite well, as well as the stability curve and the response at the non-resonant and resonant branches. Due to the jumps, some transient response occurs, which appears as an overshot in the sweep-up simulation, after the jump-up frequency.

7. Discussion

Due to the presence of several design parameters in the proposed suspension configuration, the force–displacement curve can be

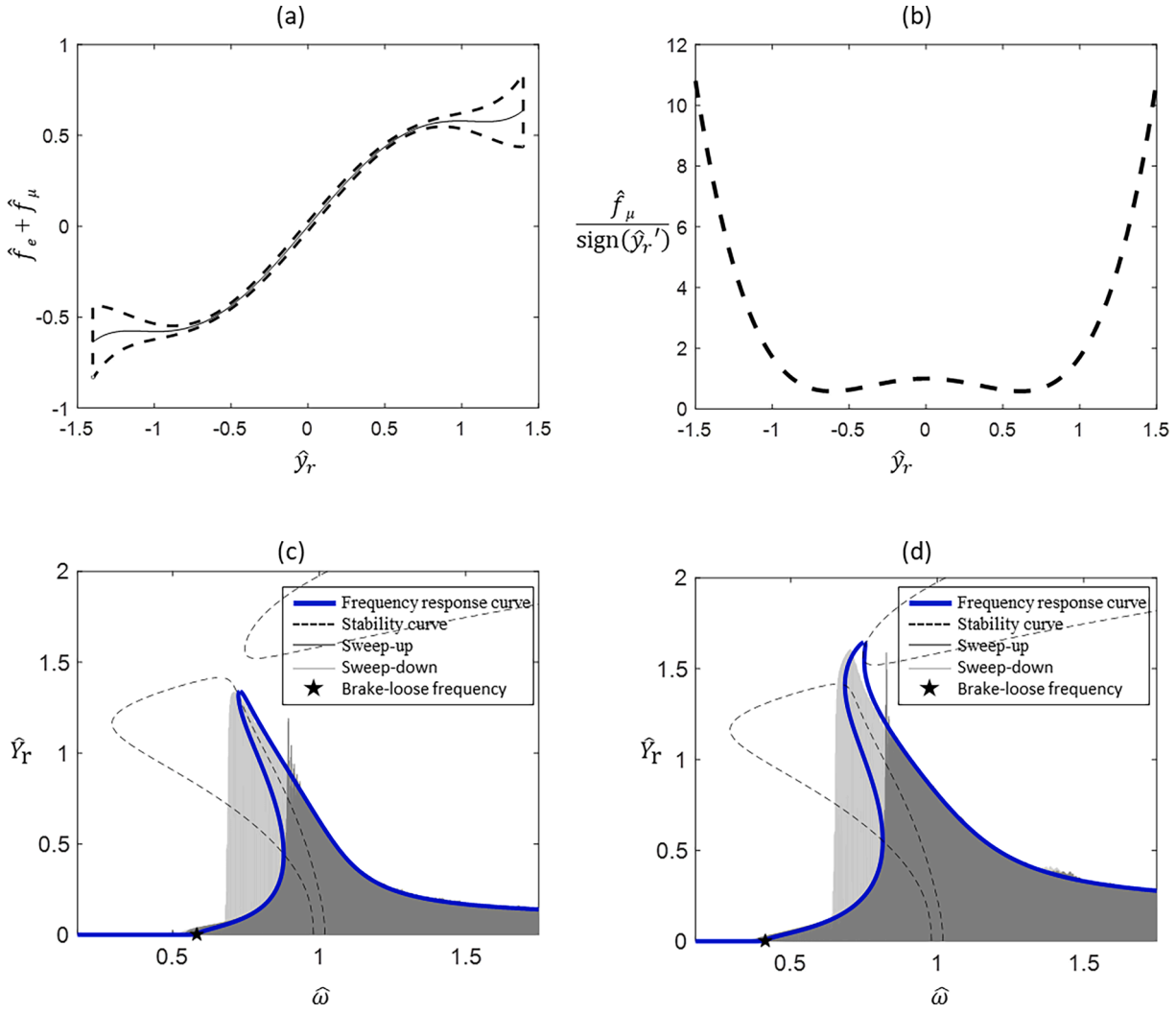

Fig. 12. Analytical results and numerical simulations of the proposed model for $\sigma = 1.06, \mu = 0.025, \widehat{\mu}_2 = -2.2, \widehat{\mu}_4 = 2.9$. (a) Elastic force and hysteresis due to friction, (b) amplitude-dependent friction coefficient, frequency response curve for (c) $\widehat{Y}_b = 0.095$ and (d) $\widehat{Y}_b = 0.19$. In (c) and (d) dashed lines are the stability curves from Eq. (39), the thin grey lines indicate numerical sweeps for validation: dark-grey trace is for the sweep-up, and light-grey trace is for the sweep-down.

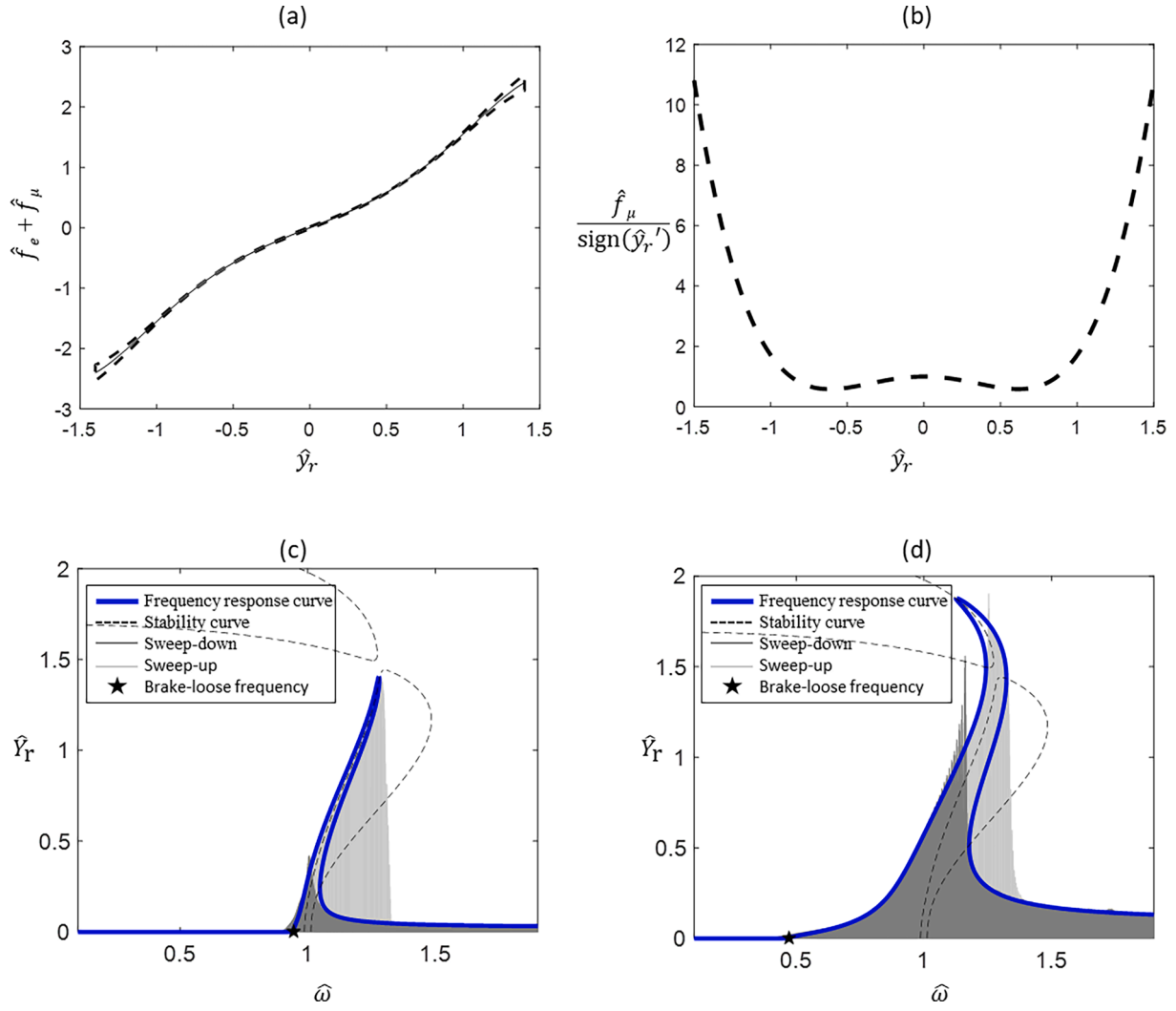

Fig. 13. Analytical results and numerical simulations of the proposed model for $\sigma = 4.23, \mu = 0.017, \hat{\mu}_2 = -2.2, \hat{\mu}_4 = 2.9$. (a) Elastic force and hysteresis due to friction, (b) amplitude-dependent friction coefficient, frequency response curve for (c) $\hat{Y}_{\mathrm{b}} = 0.024$ and (d) $\hat{Y}_{\mathrm{b}} = 0.095$. In (c) and (d) dashed lines are the stability curves from Eq. (39), the thin grey lines indicate numerical sweeps for validation: light-grey trace is for the sweep-up, and dark-grey trace is for the sweep-down.

adjusted to achieve tailored characteristics.

The focus of this paper was to achieve a quasi-linear force–displacement characteristic for large displacements, which is not so obvious given the inherently strong geometric nonlinear nature of the system. It is found that a relationship exists among the springs inclination, assembled length and free length of the springs, so that a theoretically exact linear behaviour is achieved. This interesting theoretical result was also confirmed by the experiments.

The key to achieve a linear behaviour from the inherently strong nonlinear oscillator was to adopt compression springs mounted outwards and restrained by an adjustable stopper. In fact, an exact linear behaviour is not generally achievable in purely theoretical studies that consider the spring length equal to the pin-pin distance, as shown in Fig. 14(a). Even considering the springs mounted inwards, as illustrated in Fig. 14(b), an exact linear behaviour could not be physically attained. For ease of reference and comparison, Fig. 14(c) shows the configuration proposed in this paper, where the springs are mounted outwards.

As a consequence, an equivalent linear spring can be achieved either using a classical configuration where the constitutive springs are aligned to the direction of motion, as shown at the bottom of Fig. 15(a), or using the proposed configuration where the constitutive springs are mounted outwards, inclined to the direction of motion, and having a specific free length $h_0 = h + \sqrt{a^2 + b^2}$, as shown at the top of Fig. 15(a).

By examining the force–displacement components of the two pairs of springs in the X-shaped configuration, it was theoretically found that even one single pair of springs, orthogonal to the direction of motion, can be adopted to achieve a linear behaviour. This is illustrated at the top of Fig. 15(b), where the free length is now $h_0 = h + b$, and thus compares to the classical configuration of springs

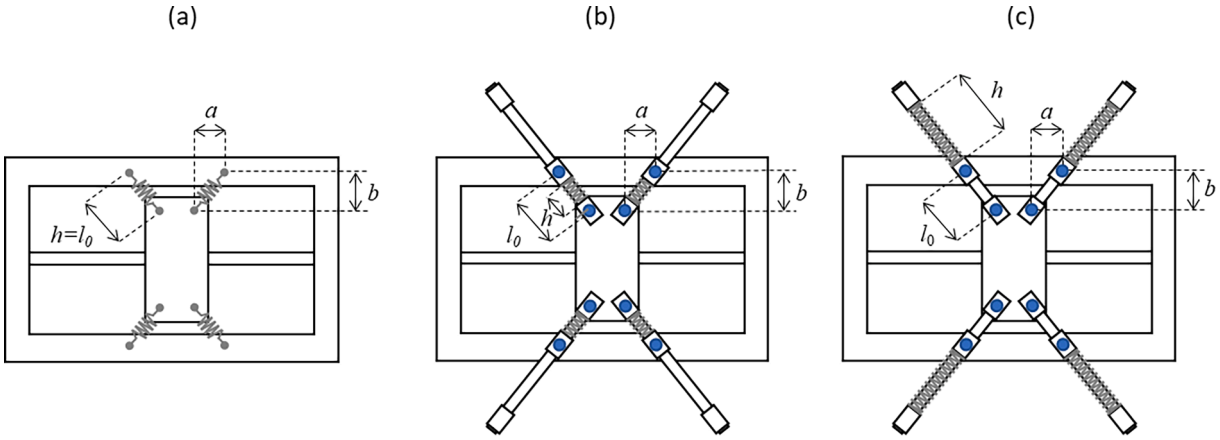

Fig. 14. Different ways to realise an X-shaped-spring configuration: (a) ideal springs, (b) springs mounted inwards, (c) springs mounted outwards (i.e., the proposed configuration).

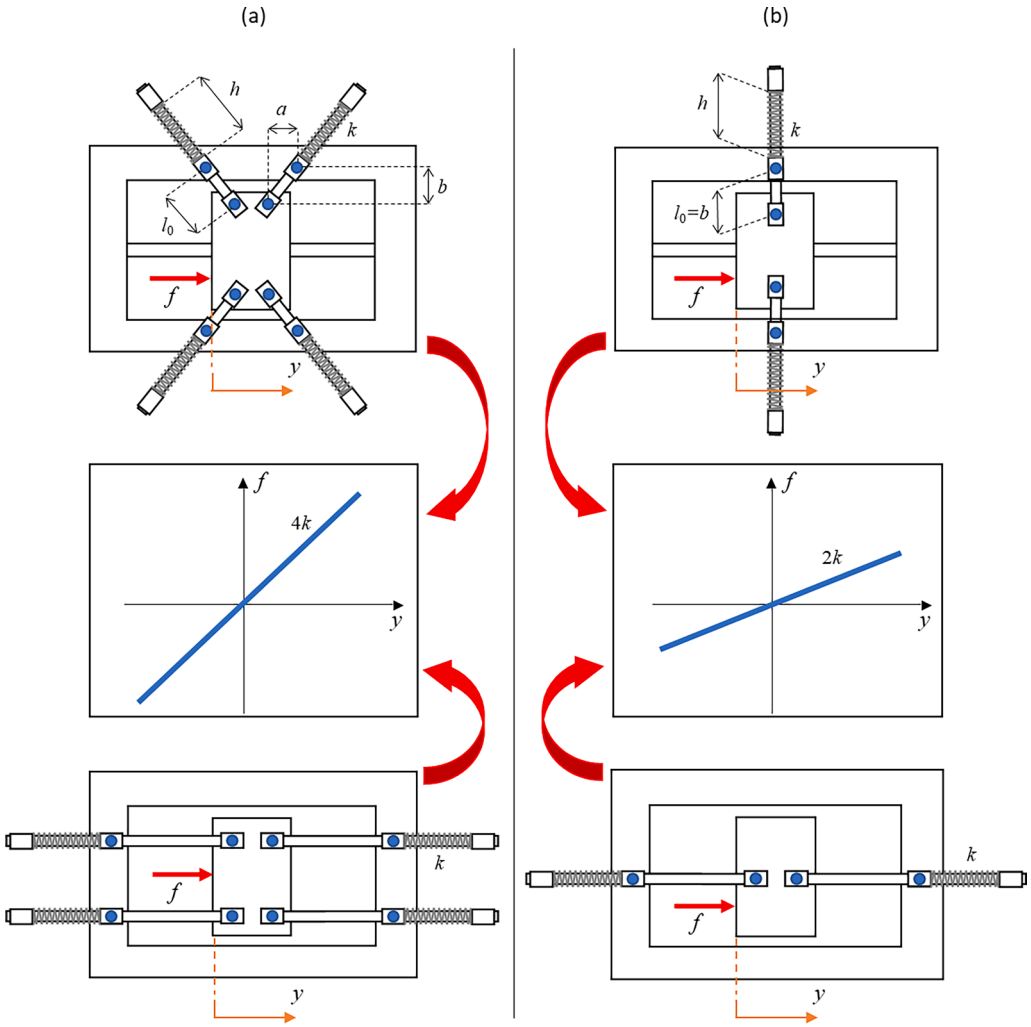

Fig. 15. Different ways to realise a linear suspension using compressed springs mounted outwards: (a) two pairs of springs, and (b) one pair of springs.

aligned to the direction of motion, illustrated at the bottom of Fig. 15(b).

The proposed configuration with four springs inclined (or two springs orthogonal) to the direction of motion, as illustrated in the top of Fig. 15(a) and 15(b), respectively, extends the possibility to realize linear engineering suspensions, and better cope with mechanical and physical constraints.

A generalised dynamic model of the nonlinear oscillator is then implemented, which considers geometrical nonlinear stiffness, geometrical nonlinear viscous friction, and geometrical nonlinear dry friction. Amplitude-dependent coefficients have been assumed, and an approximate analytic amplitude-frequency equation is obtained. This is achieved by using the method of averaging [71] in the assumption of predominantly harmonic response. Although the system was designed to behave as quasi-linear, such a detailed nonlinear model has been introduced to be able to predict and assess any deviation of the system from the designed one. It also extends the current literature when strong nonlinear behaviour is of interest, and dry friction is a dominant factor.

A prototype device was conceived and assembled to experimentally validate the theoretical design and expectations. Both static and dynamic tests were performed.

The static test was useful to uncover the amplitude dependency of the dry friction coefficient. This is believed to be due to the geometrical nonlinearity of the X-shaped architecture, which causes a variable contact force in the mechanical connections, depending on the position of the suspended mass. A clear and relatively wide hysteretic cycle was measured, whose backbone curve had indeed a quasi-linear trend. The high friction was thought to be mainly due to the plastic joint connections.

The dynamic tests were conducted by exciting the oscillator base in a harmonic fashion, at different frequencies and with different amplitudes of oscillations. Again, a quasi-linear behaviour was observed, validating the capability to design a strong nonlinear oscillator to behave in a linear-like fashion for large displacements.

8. Conclusions

This paper has investigated the static and dynamic characteristics of the nonlinear suspension of a mechanical oscillator consisting of two pairs of inclined linear springs arranged in an X-shaped configuration.

A relationship among the system parameters has been found for which the force–displacement characteristic is linear, and this reflects into the free length of the springs being related to the inclination of the springs and their assembled length.

A prototype device was built and tested for experimental validation. The static test on the prototype device suggested that friction was quite relevant, but did not follow the classical Coulomb friction model. At least one amplitude-dependent coefficient was needed, to fit the quasi-static experimental data.

This motivated the development of a much comprehensive dynamic model, respect to those adopted in the recent literature, to describe the behaviour of this class of oscillators. The dynamic tests on the prototype device confirmed the theoretical discussion. Additional analysis, on the use of the proposed model for behaviours that deviate from the linear one, is also provided and validated by numerical simulations.

This paper advances the knowledge on the characteristics of X-shaped-spring nonlinear elastic suspensions, addressing a change in the viewpoint of their sought performance, i.e., the intentional use of nonlinearity for the design of more versatile linear systems.

From a more practical engineering point of view, respect to the classical linear oscillator (with linear springs along the direction of motion), the proposed oscillator (with linear springs inclined with respect to the direction of motion), offers an alternative solution to potentially better fit different design constraints.

Funding

This research received no specific grant from any funding agency in the public, commercial, or not-for-profit sectors.

Declaration of Competing Interest

The authors declare that they have no known competing financial interests or personal relationships that could have appeared to influence the work reported in this paper.

Data availability

Data will be made available on request.

Acknowledgments

The authors wish to acknowledge the help provided by Mauro Scarparo, Carlo Brambilla, and Antonio di Natale at the mechanical workshop, Department of Physics – Polytechnic of Milan, for manufacturing some of the mechanical components of the prototype device and actuation system.

Appendix A. Supplementary data

Supplementary data to this article can be found online at https://doi.org/10.1016/j.ymssp.2023.110362.

References

[1] R.A. Ibrahim, Recent advances in nonlinear passive vibration isolators, J. Sound Vib. 314 (3–5) (2008) 371–452, https://doi.org/10.1016/j.jsv.2008.01.014.
[2] A.M. Giri, S.F. Ali, A. Arockiarajan, Dynamics of symmetric and asymmetric potential well-based piezoelectric harvesters: a comprehensive review, J. Intell. Mater. Syst. Struct. 32 (2021) 1881–1947, https://doi.org/10.1177/1045389X20978292.
[3] H. Ding, L.-Q. Chen, Designs, analysis, and applications of nonlinear energy sinks, Nonlinear Dyn. 100 (2020) 3061–3107, https://doi.org/10.1007/s11071-020-05724-1.
[4] D.F. Ledezma-Ramírez, P.E. Tapia-Gonź alez, N. Ferguson, M.J. Brennan, B. Tang, Recent advances in shock isolation: An overview and future possibilities, Applied Mechanics Reviews 71 (2019), 060802, 10.1115/1.4044190.
[5] Z. Lu, Z. Wang, Y. Zhou, X. Lu, Nonlinear dissipative devices in structural vibration control: a review, J. Sound Vib. 423 (2018) 18–49, https://doi.org/10.1016/j.jsv.2018.02.052.
[6] X. Jing, Y. Chai, X. Chao, J. Bian, In-situ adjustable nonlinear passive stiffness using X-shaped mechanisms, Mech. Syst. Sig. Process. 170 (2022), 108267, https://doi.org/10.1016/j.ymssp.2021.108267.
[7] G. Gatti, An adjustable device to adaptively realise diverse nonlinear force-displacement characteristics, Mech. Syst. Sig. Process. 180 (2022), 109379, https://doi.org/10.1016/j.ymssp.2022.109379.
[8] D.R. Nahar, T. Sugar, Compliant Constant-Force Mechanism with a Variable Output for Micro/Macro Applications, Proceedings of the 2003 lEEE International Conference on Robotics & Automation, Taipei, Taiwan, September 14-19, 2003. 10.1109/ROBOT.2003.1241615.
[9] T.D. Le, K.K. Ahn, A vibration isolation system in low frequency excitation region using negative stiffness structure for vehicle seat, J. Sound Vib. 330 (2011) 6311–6335, https://doi.org/10.1016/j.jsv.2011.07.039.
[10] X. Chong, Z. Wu, F. Li, Vibration isolation properties of the nonlinear X-combined structure with a high-static and low-dynamic stiffness: Theory and experiment, Mech. Syst. Sig. Process. 179 (2022), 109352, https://doi.org/10.1016/j.ymssp.2022.109352.
[11] Y. Yu, G. Yao, Z. Wu, Nonlinear primary responses of a bilateral supported X-shape vibration reduction structure, Mech. Syst. Sig. Process. 140 (2020), 106679, https://doi.org/10.1016/j.ymssp.2020.106679.
[12] Y. Xiong, F. Li, Y.u. Wang, A nonlinear quasi-zero-stiffness vibration isolation system with additional X-shaped structure: Theory and experiment, Mech. Syst. Sig. Process. 177 (2022), 109208, https://doi.org/10.1016/j.ymssp.2022.109208.
[13] X. Xiong, Y. Wang, J. Li, F. Li, Internal resonance analysis of bio-inspired X-shaped structure with nonlinear vibration absorber, Mech. Syst. Sig. Process. 185 (2023), 109809, https://doi.org/10.1016/j.ymssp.2022.109809.
[14] G. Gatti, Optimizing elastic potential energy via geometric nonlinear stiffness, Commun. Nonlinear Sci. Numer. Simul. 103 (2021), 106035, https://doi.org/10.1016/j.cnsns.2021.106035.
[15] J. Bian, X. Jing, Analysis and design of a novel and compact X-structured vibration isolation mount (X-Mount) with wider quasi-zero stiffness range, Nonlinear Dyn. 101 (2020) 2195–2222, https://doi.org/10.1007/s11071-020-05878-y.
[16] Y. Chai, X. Jing, X. Chao, X-shaped mechanism based enhanced tunable QZS property for passive vibration isolation, Int. J. Mech. Sci. 218 (2022), 107077, https://doi.org/10.1016/j.ijmecsci.2022.107077.
[17] X. Jing, L. Zhang, G. Jiang, X. Feng, Y. Guo, Z. Xu, Critical factors in designing a class of X-shaped structures for vibration isolation, Eng. Struct. 199 (2019), 109659, https://doi.org/10.1016/j.engstruct.2019.109659.
[18] Y. Wang, X. Jing, Nonlinear stiffness and dynamical response characteristics of an asymmetric X-shaped structure, Mech. Syst. Sig. Process. 125 (2019) 142–169, https://doi.org/10.1016/j.ymssp.2018.03.045.
[19] J. Bian, X. Jing, A nonlinear X-shaped structure based tuned mass damper with multi-variable optimization (X-absorber), Commun. Nonlinear Sci. Numer. Simul. 99 (2021), 105829, https://doi.org/10.1016/j.cnsns.2021.105829.
[20] Y. Li, H. Li, X. Liu, S. Yan, Bandgap and wave propagation of spring–mass–truss elastic metamaterial with a scissor-like structure, J. Phys. D Appl. Phys. 55 (2022), 055303, https://doi.org/10.1088/1361-6463/ac2fd7.
[21] G. Yan, H.-X. Zou, S. Wang, L.-C. Zhao, Q.-H. Gao, T. Tan, W.-M. Zhang, Large stroke quasi-zero stiffness vibration isolator using three-link mechanism, J. Sound Vib. 478 (2020), 115344, https://doi.org/10.1016/j.jsv.2020.115344.
[22] J. Bian, X. Jing, Superior nonlinear passive damping characteristics of the bio-inspired limb-like or X-shaped structure, Mech. Syst. Sig. Process. 125 (2019) 21–51, https://doi.org/10.1016/j.ymssp.2018.02.014.
[23] G. Jiang, X. Jing, Y. Guo, A novel bio-inspired multi-joint anti-vibration structure and its nonlinear HSLDS properties, Mech. Syst. Sig. Process. 138 (2020), 106552, https://doi.org/10.1016/j.ymssp.2019.106552.
[24] M.-Q. Niu, L.-Q. Chen, Analysis of a bio-inspired vibration isolator with a compliant limb-like structure, Mech. Syst. Sig. Process. 179 (2022), 109348, https://doi.org/10.1016/j.ymssp.2022.109348.
[25] G. Yan, W.-H. Qi, J.-W. Shi, H. Yan, H.-X. Zou, L.-C. Zhao, Z.-Y. Wu, X.-Y. Fang, X.-Y. Li, W.-M. Zhang, Bionic paw-inspired structure for vibration isolation with novel nonlinear compensation mechanism, J. Sound Vib. 525 (2022), 116799, https://doi.org/10.1016/j.jsv.2022.116799.
[26] G. Yan, H.-X. Zou, S. Wang, L.-C. Zhao, Z.-Y. Wu, W.-M. Zhang, Bio-inspired toe-like structure for low-frequency vibration isolation, Mech. Syst. Sig. Process. 162 (2022), 108010, https://doi.org/10.1016/j.ymssp.2021.108010.
[27] P. Ling, L. Miao, W. Zhang, C. Wu, B. Yan, Cockroach-inspired structure for low-frequency vibration isolation, Mech. Syst. Sig. Process. 171 (2022), 108955, https://doi.org/10.1016/j.ymssp.2022.108955.
[28] H. Dai, X. Jing, Y. Wang, X. Yue, J. Yuan, Post-capture vibration suppression of spacecraft via a bio-inspired isolation system, Mech. Syst. Sig. Process. 105 (2018) 214–240, https://doi.org/10.1016/j.ymssp.2017.12.015.
[29] G. Yan, H.-X. Zou, S. Wang, L.-C. Zhao, Z.-Y. Wu, W.-M. Zhang, Bio-Inspired Vibration Isolation: Methodology and Design, Appl. Mech. Rev. 73 (2021), 020801, https://doi.org/10.1115/1.4049946.
[30] A.D. Shaw, G. Gatti, P.J.P. Gonçalves, B. Tang, M.J. Brennan, Design and test of an adjustable quasi-zero stiffness device and its use to suspend masses on a multi-modal structure, Mech. Syst. Sig. Process. 152 (2021), 107354, https://doi.org/10.1016/j.ymssp.2020.107354.
[31] A. Carrella, M.J. Brennan, T.P. Waters, Static analysis of a passive vibration isolator withquasi-zero-stiffness characteristic, J. Sound Vib. 301 (2007) 678–689, https://doi.org/10.1016/j.jsv.2006.10.011.
[32] G. Gatti, Statics and dynamics of a nonlinear oscillator with quasi-zero stiffness behaviour for large deflections, Commun. Nonlinear Sci. Numer. Simul. 83 (2020), 105143, https://doi.org/10.1016/j.cnsns.2019.105143.
[33] G. Gatti, A K-shaped spring configuration to boost elastic potential energy, Smart Mater. Struct. 28 (2019), 077002, https://doi.org/10.1088/1361-665X/ab1ec8.
[34] F. Zhao, J.C. Ji, K. Ye, Q. Luo, Increase of quasi-zero stiffness region using two pairs of oblique springs, Mech. Syst. Sig. Process. 144 (2020), 106975, https://doi.org/10.1016/j.ymssp.2020.106975.
[35] F. Zhao, J. Ji, Q. Luo, S. Cao, L. Chen, W. Du, An improved quasi-zero stiffness isolator with two pairs of oblique springs to increase isolation frequency band, Nonlinear Dyn. 104 (2021) 349–365, https://doi.org/10.1007/s11071-021-06296-4.
[36] F. Zhao, J. Ji, K. Ye, Q. Luo, An innovative quasi-zero stiffness isolator with three pairs of oblique springs, Int. J. Mech. Sci. 192 (2021), 106093, https://doi.org/10.1016/j.ijmecsci.2020.106093.
[37] F. Zhao, S. Cao, Q. Luo, J. Ji, Enhanced design of the quasi-zero stiffness vibration isolator with three pairs of oblique springs: Theory and experiment, J. Vib. Control*In Press* (2022), https://doi.org/10.1177/10775463221074143.
[38] T. Yang, Q. Cao, Dynamics and performance evaluation of a novel tristable hybrid energy harvester for ultra-low level vibration resources, Int. J. Mech. Sci. 156 (2019) 123–136, https://doi.org/10.1016/j.ijmecsci.2019.03.034.
[39] Q.J. Cao, Y.W. Han, T.W. Liang, M. Wiercigroch, S. Piskarev, Multiple Buckling and Codimension-Three Bifurcation Phenomena of a Nonlinear Oscillator, Int. J. Bifurcation Chaos 24 (1) (2014) 1430005, https://doi.org/10.1142/S0218127414300055.

[40] B. Zhou, Y. Jin, H. Xu, Subharmonic resonance and chaos for a class of vibration isolation system with two pairs of oblique springs, App. Math. Model. 108 (2022) 427–444, https://doi.org/10.1016/j.apm.2022.03.021.
[41] B. Yan, N. Yu, H. Ma, C. Wu, A theory for bistable vibration isolators, Mech. Syst. Sig. Process. 167 (2022), 108507, https://doi.org/10.1016/j.ymssp.2021.108507.
[42] B. Yan, H. Ma, L. Zhang, W. Zheng, K. Wang, C. Wu, A bistable vibration isolator with nonlinear electromagnetic shunt damping, Mech. Syst. Sig. Process. 136 (2020), 106504, https://doi.org/10.1016/j.ymssp.2019.106504.
[43] Q. Cao, Y. Xiong, M. Wiercigroch, A novel model of dipteran flight mechanism, Int. J. Dyn. Control 1 (2013) 1–11, https://doi.org/10.1007/s40435-013-0001-5.
[44] Q. Cao, M. Wiercigroch, E.E. Pavlovskaia, C. Grebogi, J.M.T. Thompson, Archetypal oscillator for smooth and discontinuous dynamics, Phys. Rev. E 74 (2006), 046218, https://doi.org/10.1103/PhysRevE.74.046218.
[45] Z. Wu, X. Jing, B. Sun, F. Li, A 6DOF passive vibration isolator using X-shape supporting structures, J. Sound Vib. 380 (2016) 90–111, https://doi.org/10.1016/j.jsv.2016.06.004.
[46] G. Zhu, Q. Cao, Z. Wang, Y. Zhang, Y. Chen, K.-C. Woo, Road to entire insulation for resonances from a forced mechanical system, Sci. Rep. 12 (2022) 21167, https://doi.org/10.1038/s41598-022-25691-4.
[47] A. Mojahed, K. Moore, L.A. Bergman, A.F. Vakakis, Strong geometric softening–hardening nonlinearities in an oscillator composed of linear stiffness and damping elements, Int. J. Non Linear Mech. 107 (2018) 94–111, https://doi.org/10.1016/j.ijnonlinmec.2018.09.004.
[48] G. Gatti, D.F. Ledezma-Ramirez, M.J. Brennan, Performance of a shock isolator inspired by skeletal muscles, Int. J. Mech. Sci. 244 (2023), 108066, https://doi.org/10.1016/j.ijmecsci.2022.108066.
[49] Gatti, G., Svelto, C. (2022). Performance of a vibration isolator with sigmoidal force-deflection curve. Journal of Vibration and Control *in press* (2022). 10.1177/10775463221139006.
[50] D. Zou, G. Liu, Z. Rao, T. Tan, W. Zhang, W.-H. Liao, A device capable of customizing nonlinear forces for vibration energy harvesting, vibration isolation, and nonlinear energy sink, Mech. Syst. Sig. Process. 147 (2021), 107101, https://doi.org/10.1016/j.ymssp.2020.107101.
[51] Z. Wu, W. Liu, F. Li, C. Zhang, Band-gap property of a novel elastic metamaterial beam with X-shaped local resonators, Mech. Syst. Sig. Process. 134 (2019), 106357, https://doi.org/10.1016/j.ymssp.2019.106357.
[52] B. Tang, M.J. Brennan, A comparison of two nonlinear damping mechanisms in a vibration isolator, J. Sound Vib. 332 (2013) 510–520, https://doi.org/10.1016/j.jsv.2012.09.010.
[53] G. Yan, Z.-Y. Wu, X.-S. Wei, S. Wang, H.-X. Zou, L.-C. Zhao, W.-H. Qi, W.-M. Zhang, Nonlinear compensation method for quasi-zero stiffness vibration isolation, J. Sound Vib. 523 (2022), 116743, https://doi.org/10.1016/j.jsv.2021.116743.
[54] H.T. Yang, I.Y. Kwon, C.J. Randall, P.K. Hansma, F.S. Ly, Preliminary design, experiment, and numerical study of a prototype hydraulic bio-inspired damper, J. Sound Vib. 459 (2019), 114845, https://doi.org/10.1016/j.jsv.2019.07.011.
[55] X. Gao, H.D. Teng, Dynamics and nonlinear effects of a compact near-zero frequency vibration isolator with HSLD stiffness and fluid damping enhancement, Int. J. Non Linear Mech. 128 (2021), 103632, https://doi.org/10.1016/j.ijnonlinmec.2020.103632.
[56] B. Ravindra, K. Mallik, Hard duffing-type vibration isolator with combined coulomb and viscous damping, Int. J. Nonlinear Mech. 28 (1993) 427–440, https://doi.org/10.1016/0020-7462(93)90017-F.
[57] G. Gatti, A.D. Shaw, P.J.P. Gonçalves, M.J. Brennan, On the detailed design of a quasi-zero stiffness device to assist in the realisation of a translational Lanchester damper, Mech. Syst. Sig. Process. 164 (2022), 108258, https://doi.org/10.1016/j.ymssp.2021.108258.
[58] X. Liu, Q. Zhao, Z. Zhang, X. Zhou, An experiment investigation on the effect of Coulomb friction on the displacement transmissibility of a quasi-zero stiffness isolator, J. Mech. Sci. Technol. 33 (1) (2019) 121–127, https://doi.org/10.1007/s12206-018-1212-7.
[59] A. Donmez, E. Cigeroglu, G.O. Ozgen, An improved quasi-zero stiffness vibration isolation system utilizing dry friction damping, Nonlinear Dyn. 101 (2020) 107–121, https://doi.org/10.1007/s11071-020-05685-5.
[60] R. Zhu, S. Marchesiello, D. Anastasio, D. Jiang, Q. Fei, Nonlinear system identification of a double-well Duffing oscillator with position-dependent friction, Nonlinear Dyn. 108 (2022) 2993–3008, https://doi.org/10.1007/s11071-022-07346-1.
[61] L. Marino, A. Cicirello, Experimental investigation of a single-degree-of-freedom system with Coulomb friction, Nonlinear Dyn. 99 (2020) 1781–1799, https://doi.org/10.1007/s11071-019-05443-2.
[62] J. Wojewoda, A. Stefanski, M. Wiercigroch, T. Kapitaniak, Hysteretic effects of dry friction: modelling and experimental studies, Phil. Trans. R. Soc. A 366 (2008) 747–765, https://doi.org/10.1098/rsta.2007.2125.
[63] M.J. Brennan, G. Gatti, Harvesting energy from time-limited harmonic vibrations: mechanical considerations, J. Vib. Acoust. 139 (2017), 051019, https://doi.org/10.1115/1.4036867.
[64] V.G. Cleante, M.J. Brennan, G. Gatti, D.J. Thompson, Energy harvesting from the vibrations of a passing train: Effect of speed variability, J. Phys. Conf. Ser. 744 (2016), 012080, https://doi.org/10.1088/1742-6596/744/1/012080.
[65] Z.Q. Lang, X.J. Jing, S.A. Billings, G.R. Tomlinson, Z.K. Peng, Theoretical study of the effects of nonlinear viscous damping on vibration isolation of sdof systems, J. Sound Vib. 323 (2009) 352–365, https://doi.org/10.1016/j.jsv.2009.01.001.
[66] Y.-P. Zhu, Z.Q. Lang, Beneficial effects of antisymmetric nonlinear damping with application to energy harvesting and vibration isolation under general inputs, Nonlinear Dyn. 108 (2022) 2917–2933, https://doi.org/10.1007/s11071-022-07444-0.
[67] S.J. Elliott, M.G. Tehrani, R.S. Langley, Nonlinear damping and quasi-linear modelling, Philos. Trans. R. Soc. A Math. Phys. Eng. Sci. 373 (2015) 20140402, https://doi.org/10.1098/rsta.2014.0402.
[68] J.S. Love, T.C. Haskett, The practical effects of friction for tuned mass dampers installed in tall buildings, Eng. Struct. 265 (2022), 114495, https://doi.org/10.1016/j.engstruct.2022.114495.
[69] G. Gatti, Effect of parameters on the design of a suspension system with four oblique springs, Shock Vib. (2021) 5556088, https://doi.org/10.1155/2021/5556088.
[70] G. Gatti, M.J. Brennan, B. Tang, Some diverse examples of exploiting the beneficial effects of geometric stiffness nonlinearity, Mech. Syst. Sig. Process. 125 (2019) 4–20, https://doi.org/10.1016/j.ymssp.2018.08.024.
[71] A.H. Nayfeh, Perturbation Methods. Wiley-Vch Verlag GmbH & Co. KGaA, Weinheim, 2004. 10.1002/9783527617609.